Gallo, Pasquale; Lehto, Pauli; Malitckii, Evgenii; Remes, Heikki

Influence of microstructural deformation mechanisms and shear strain localisations on small fatigue crack growth in ferritic stainless steel

Published in:
International Journal of Fatigue

DOI:
10.1016/j.ijfatigue.2022.107024

Published: 01/10/2022

Document Version
Publisher's PDF, also known as Version of record

Please cite the original version:
Gallo, P., Lehto, P., Malitckii, E., & Remes, H. (2022). Influence of microstructural deformation mechanisms and shear strain localisations on small fatigue crack growth in ferritic stainless steel. *International Journal of Fatigue*, *163*, Article 107024. https://doi.org/10.1016/j.ijfatigue.2022.107024

International Journal of Fatigue 163 (2022) 107024

Contents lists available at ScienceDirect

International Journal of Fatigue

journal homepage: www.elsevier.com/locate/ijfatigue

Influence of microstructural deformation mechanisms and shear strain localisations on small fatigue crack growth in ferritic stainless steel

P. Gallo [*], P. Lehto, E. Malitckii, H. Remes

Aalto University, Department of Mechanical Engineering, Otakaari 4, 02150 Espoo, Finland

ARTICLE INFO

Keywords:
Digital image correlation
Short cracks
Domain misorientation
Crack growth rate
Strain localisation

ABSTRACT

Microstructurally small fatigue crack growth (FCG) rate in body-centred cubic (BCC) ferritic stainless steel is investigated by using a novel domain misorientation approach for EBSD microstructural deformation analyses, in conjunction with in situ digital imaging correlation (DIC). The DIC analyses revealed that shear strain localisations occur ahead of the crack tip during propagation and correlate well with the FCG rate retardations. Grain boundaries can be found at both peaks and valleys of the FCG rate curve and alter the interaction between crack growth and shear strain localisations. At the microstructural level, the deformation is associated with the dislocation-mediated plastic deformation process, showing increased formation of grain sub-structures in the regions of the strain localisation. Consequently, material experiences local hardening causing the FCG retardation events. If the crack avoids the hardened material region through a macroscopic cross-slip mechanism, retardation is minor. On the contrary, if the crack penetrates the hardened region, retardation is significant.

1. Introduction

The majority of classical concepts and numerical methods for the fatigue assessment of engineering components made of steel were originally developed by considering macro-scale aspects and cracks that are relatively large compared to the microstructural scale. The microstructural effect was then averaged by appropriate constitutive laws, or the crack growth modelling did not interact at all with the microstructure. Recent literature suggests that in many applications, such as ships and bridges, where the employment of high-strength materials and very thin plates is increasing in order to achieve weight reduction, cracks spend most of their lifetimes at the microstructural level and may be heavily influenced by the microstructure or local imperfections [1–4]. Thus, investigation and understanding of crack growth from the smallest size until final failure may be useful in characterising the development of fatigue damage in those complex structures [5], where classic empirical models fail. Small-scale defects are often referred to as “small cracks” or “short cracks”, and it is not uncommon to see these terms used as synonyms. For the sake of clarity, in the present work we prefer to distinguish among these two terms as [6]:

- small crack: when all its dimensions are similar to or smaller than the largest microstructural feature;
- short crack: only one dimension is large compared to the microstructural features.

Additionally, several definitions and classifications of small cracks can be found in the literature [7]. In the present work, the focus is on microstructurally small cracks: fatigue cracks that are small compared to the scale of the microstructural dimension, e.g. grain size [7].

Small cracks have been shown to behave in a profoundly different way from long cracks [8,9]. Early works suggested that these differences were due to a complex interaction of several factors ahead of (primary events) and behind (secondary events) the crack tip [10,11]. In the past few decades, many researchers have focused on the behaviour of small cracks, providing copious experimental data and insights, and proposing a variety of engineering models [12–15]. Computational frameworks for small crack propagation have also seen interesting new developments by proposing a completely new level of integration [16], and going so far as to rely on machine learning and data-driven approaches [17]. Unsurprisingly, sometimes experimental evidence shows opposite and contrasting effects on the fatigue threshold and the growth kinetics [18], causing challenges in the simulation of small crack behaviour using fracture mechanics [19].

Until recently, the lack of in situ experimental tools to extract adequate full-field and microstructural information in the proximity of

---

[*] Corresponding author.
E-mail address: pasquale.gallo@aalto.fi (P. Gallo).

https://doi.org/10.1016/j.ijfatigue.2022.107024
Received 4 March 2022; Received in revised form 10 May 2022; Accepted 19 May 2022

the crack tip had been the main obstacle to further significant developments. In the past few years, high-resolution full-field measurement tools such as digital image correlation (DIC) have become reliable and widely available. These new tools finally provide the possibility of investigating in situ local deformation and the crack driving force under cyclic loading at a microstructural level [20–22]. The microstructural evolution ahead of a small crack, that has been shown to often dominate the early propagation stage [23], can also be studied in detail with the measurement of plastic strain accumulation and microstructural changes through Electron Backscatter Diffraction (EBSD) techniques [24–26]. Significant effort has been devoted to understanding the nature and origins of the deformation heterogeneities at the microstructural level. In polycrystalline materials the grain boundaries both restrict the rotation of the crystal lattice and inhibit the motion of dislocations [27,28]. The pile-up of dislocations at grain boundaries [29] is a fundamental strengthening mechanism for many engineering materials, known as the Hall-Petch relationship [30,31]. Thus, the dislocation density increases inside the grains, causing material hardening [32]. For polycrystalline BCC materials the dislocations typically re-arrange, forming dense dislocation walls and dislocation cells, which evolve into sub-grains and new grains as deformation progresses [33]. Size of these microstructural deformation patterns typically ranges from several micrometres to the sub-micrometre regime, with size being inversely proportional to the plastic strain accumulation [34,35].

The importance of plastic strain accumulation and localisation on fatigue crack growth is reported in several recent works. Carroll et al. [36,37] investigated the interactions between plastic strain accumulation, microstructure, and fatigue crack behaviour at the sub-grain level. The mapped plastic strain accumulation was found to be quite inhomogeneous at the microstructural level, and strain localisation was associated with slip bands within grains and at twin grain boundaries. The local crack path and fatigue crack growth (FCG) rate were shown to depend on the microstructure and a favourable orientation to slip, but also on strain accumulation. Jiang et al. [38] presented a characterisation of strain localisation at the grain level during fatigue crack initiation (and early propagation) by combining SEM and DIC analyses in an advanced Ni-based superalloy. The results showed that cracks preferentially initiate from slip/strain bands adjacent and parallel to twin boundaries, and then propagate along the slip/strain bands; crack propagation was closely related to strain accumulation ahead of the crack tip. Some recent studies show that a microstructurally sensitive stored energy density can be used as mechanistic driver for small, short crack growth and crack initiation. The stored energy density also enabled the determination of a critical crack length for microstructural sensitivity [39–41]. Furthermore, Malitckii et al. [42] showed the importance of strain localisation for microstructurally small FCG. By means of in situ DIC measurements, the variation in the FCG rate was found to correlate better with the shear strain localisation than the grain boundaries.

Although these recent works have brought significant new understanding of microstructurally small fatigue crack, we still have limited knowledge about the mutual relation between the microstructural deformation mechanisms, formation of grain sub-structures, shear strain localizations and crack growth behavior. To fill this gap, the current work focuses on microstructurally small FCG by considering local features, i.e. grain boundaries, microstructural deformation patterns, and local mechanisms such as strain localisation. The target is to provide a better understanding of the mechanisms behind interaction of strain localisation, microstructural features and FCG, and to discuss FCG rate retardations in light of those mechanisms. Important information on strain localisation and crack growth is obtained by means of DIC improved by an optimised speckle pattern for higher resolution, while the evolution of microstructural deformation patterns are revealed by the novel adaptive domain misorientation approach for EBSD measurements recently proposed by Lehto [24]. Through the microstructural analyses, we aim to bridge FCG rate variations to the formation of grain sub-structures induced by shear strain localisations. The focus is on crack growth in the first few grains to deepen understanding of early interaction with microstructure.

2. Experimental methods

2.1. Material and fatigue test

A double-edge notch sample made of ferritic stainless steel ASTM UNS S43940 with 18% chromium [42] was realised by electrical discharge machining (EDM) from an annealed plate (1 h at 1200 °C in nitrogen atmosphere, quenched in water). The final average grain size of the plate, because of the thermal treatment, was increased to 349 μm without extensive formation of chromium carbides. Both surfaces of the specimen were polished to EBSD quality prior to the experiments. The sample geometry is depicted schematically in Fig. 1. The notch has an opening angle of 90°, a notch depth of 0.44 mm, and a notch root radius of 0.2 mm. This configuration results in a stress concentration factor of 2.96. It should be noted that the presence of the notch could affect the sample stress field leading to local yielding and influence the FCG process around the notch region. For this reason, the notch is designed to limit the stress concentration effect (inevitably present) to a very small region close to the notch root (i.e. very steep stress gradient in comparison to grain size). As will be illustrated later, findings from EBSD and deformation analyses confirmed indeed that the notch effect did not have significant influence on FCG process. Before pre-cracking, the sample has a net section of 2.62 mm. After pre-cracking, a through-crack a is obtained at one of the two notches, consisting of the notch depth and the physical crack l stemming from the original notch root. The thickness of the sample was 1 mm. According to the tensile test reported in [42], the Young's modulus E is equal to 210 GPa, with a yield strength, σ_{ys}, and ultimate strength, σ_{UTS}, of approximately 370 MPa and 490 MPa, respectively.

For the realisation of the pre-crack, the sample is subjected to uniaxial cyclic loading at a loading ratio $R = -0.16$, with $\sigma_{max} = 300$ MPa on the net cross-sectional area and a test frequency of 10 Hz. The negative loading ratio permits to increase the stress range without increasing the σ_{max} and to obtain the pre-crack in a reasonable time. Indeed, σ_{max} must be kept smaller than the value used in the subsequent fatigue tests after pre-cracking to avoid possible monotonic loading induced plasticity effect at the notch root. During the pre-cracking procedure, the initial crack length is checked at intervals of approximately 2000–3000 cycles by means of an optical microscope until through pre-crack detection. This procedure generated a physical through-crack l (stemming from the notch; see Fig. 1) of about 20 μm in length, i.e. 6% of the average grain size, after about 10,000 cycles. This pre-crack length assures that there is negligible influence of the damaged layer left by the EDM along the thickness direction at the notch root. This is also later confirmed by the deformation analyses (see Fig. 8) showing that the damaged layer is indeed smaller than the pre-crack obtained.

The basic principle of DIC is to compare two digital images of the specimen surface before and after deformation. Usually, a random speckle pattern is sprayed on the surface so that small regions of the specimen can be tracked and compared in different images [20]. For large samples or components, this procedure generates very good results. However, when the sample size is reduced or when phenomena on a local small scale are considered, the sprayed random speckle pattern may not provide appropriate resolution. For this reason, an optimised speckle pattern for higher resolution is employed instead. An example of the pattern is provided in Fig. 1, while the theoretical background on this novel class of strain sensor patterns can be found in the given references [43,44]. The characteristic size of the speckle pattern required for DIC calculations is approximately 10 μm [43]. The speckles are applied to the sample surface by using a silicon stamp and checked by using an optical microscope [45].

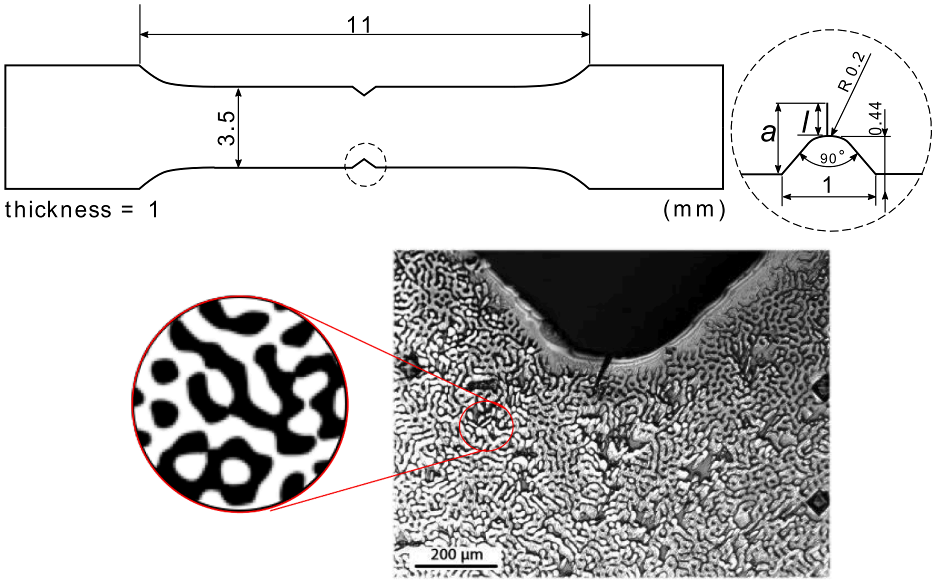

Fig. 1. Not-to-scale sketch of the fatigue test sample and example of the optimised high-resolution speckle pattern used for the investigation of a microstructurally small fatigue crack by DIC; a small fatigue crack *l* is stemming from the notch root.

After application of the pattern, a load-controlled fatigue test is conducted at a loading ratio $R = 0.1$, with $\sigma_{max} = 350$ MPa on the net cross-sectional area and a test frequency of 10 Hz. The sample is monitored during the test by an optical microscope with a 16 × precision zoom lens equipped with a digital camera with a resolution of 2048 × 1536 pixels and a field of view of 3600×2700 μm^2, resulting in spatial resolution of approximately 1.76 μm/pixel. Pictures are taken at intervals of 500 cycles during temporary stops of 10 s at an average load of approximately 210 MPa. The frame captured after the first 500 cycles was chosen to be the reference frame and thus only the increment of plastic deformation due to cyclic loading was analysed. The DIC analysis was performed using the commercial LaVision software (DaVis 8.3.1). The raw images were processed using a Least-Square Matching (LSM) algorithm with a subset (i.e. *facet*) and a step size of 17×17 pixels^2 and 5 pixels, respectively.

2.2. Analyses of fatigue crack growth (FCG) rate

The DIC images generated as explained in the previous section were carefully analysed to obtain a robust data set for microstructural level analysis. Particular attention was paid to the determination of the crack tip location. In total, ten series of crack length measurements were realised. For each series, the crack length was detected every 2500 cycles, which is found to provide a reasonably appreciable crack growth, especially at an early stage. The largest and smallest individual crack lengths are then excluded from the measurements series and the arithmetic mean is used to obtain the final crack length.

The analysis of the crack lengths to obtain the FCG rate also requires special considerations. Indeed, to capture local microstructural effects, the minimum interval between successive crack size measurements Δa is kept very small compared to traditional long crack growth tests. When Δa decreases, the relative contribution of the measurement error to the calculation of da/dN increases. For these reasons, instead of the traditional direct secant method, the incremental polynomial regression is used to evaluate the FCG rate, as recommended in [46]. The method consists of fitting a second-order polynomial to $(2n + 1)$ successive data points, where n is equal to four in the current study, that is, nine successive data points. In other words, the data is locally smoothened before calculation of FCG rate. The form of the equation for the local fit is:

$$\hat{a}_i = b_0 + b_1\left(\frac{N_i - C_1}{C_2}\right) + b_2\left(\frac{N_i - C_1}{C_2}\right)^2 \tag{1}$$

where.

$$-1 \leq \left(\frac{N_i - C_1}{C_2}\right) \leq +1 \tag{2}$$

and b_0, b_1, and b_2 are the regression parameters determined by the least square method over the crack range $a_{i\text{-}n} \leq a \leq a_{i+n}$; $\hat{a}_i$ is the fitted crack length at the number of cycles N_i; $C_1{=}(N_{i\text{-}n} + N_{i+n})/2$ and $C_2{=}(N_{i+n} - N_{i\text{-}n})/2$ are parameters used to scale the data to avoid numerical difficulties. The FCG rate at N_i is then obtained by the derivative of the above parabola. The method and all calculations are implemented in the MATLAB® software [47]. As in most of the commercial software for data analyses, the data scaling for numerical optimisation is managed automatically (e.g. see the MATLAB® Curve Fitting Toolbox [48]) and the parameters C_1 and C_2 can therefore be omitted. It should be noted that other methods are available for removing variability from the data, such as that suggested in [49,50].

2.3. Microstructure and damage analyses

The average grain size of the sample is 349 μm. The grain size analysis was carried out with the intercept length methods [51,52], available as open source in [53,54]. The DIC monitored surface was characterized using EBSD in three stages: 1) Before the fatigue test, 2) After the fatigue test was interrupted at the crack length of approximately 0.7 mm, and 3) After final failure and complete separation of the cross-section ligament. The EBSD datasets before and after the fatigue tests are used to characterise the initial microstructure and the deformation-induced changes. The high resolution EBSD datasets after final failure are used instead to study the microstructural deformation process in detail. To enhance the quality of the near crack edge analyses, the specimen was coated with an electroless nickel plating process [55] after final failure. The nickel-plated material section was polished according to standard procedures and finalised by colloidal silica polishing in a vibratory polisher to minimise the deformation induced by the sample preparation process. For the sake of brevity, a detailed description of polishing and subsequent EBSD measurements is presented in Appendix A.

Microstructural deformation patterns were analysed using the adaptive domain misorientation approach of Lehto [24], available as open source in [24,56]. This novel method can resolve sub-grains and dislocation cells using conventional EBSD by employing measurement domains that are grown radially until a specified misorientation threshold $\Delta\theta$ has been reached. In the current study, the dislocation cells are measured with the criterion $\Delta\theta = 0.5^\circ$, while $\Delta\theta = 2^\circ$ was used to measure the sub-grain size and the general extent of deformation; for further details refer to [24]. The used initial kernel size was up to 240 nearest neighbours ($481 \times 481 = 231361$ data points).

The crack growth directions were analysed to find correspondence with the crystallographic directions. Several researchers have shown that the slow-moving screw dislocations control the deformation process for ferritic BCC steel at room temperature, see e.g. [57]. For a screw dislocation with a $[11\overline{1}]$-type slip direction, the screw dislocation can propagate in any of the three $\{110\}$ and three $\{211\}$ planes of the $[11\overline{1}]$ zone axis [58], shown in Fig. 2. The crack is assumed to propagate in the direction of dislocation motion, with cross-slip between neighbouring slip planes enabling direction changes, as shown schematically in Fig. 2a. The vectors for direction of dislocation motion lie in the $\{11\overline{1}\}$-type plane; see Fig. 2c. For example, in the $(101)[11\overline{1}]$ slip system the direction of the dislocation motion is either $[\overline{1}21]$ or $[1\overline{2}\overline{1}]$; see Fig. 2b,c. In total, there are four possible combinations of six slip systems for the screw dislocation to propagate in BCC materials. The activation of a slip system is determined by the direction of stress, expressed as the maximum resolved shear stress plane (MRSSP) [58]. The active slip systems are determined by assessing the Schmid factors of the four $\langle 11\overline{1}\rangle$ slip directions and visually comparing the crack growth directions to the directions of dislocation motion. Because the Schmid factor is strictly valid only for single crystalline FCC materials [59], it is used here qualitatively to assess how favourably a specific slip system is aligned to the MRSSP and to determine the slip direction that offers multiple favourably oriented slip planes for a screw dislocation. We assume that the MRSSP is aligned with the tensile axis and that it is a suitable simplification for Stage I crack growth; linear-elastic 2D finite element analyses (FEA) showed that the principal stress direction is within $\pm 5^\circ$ of the tensile axis for the investigated crack length range. The estimation of 3D elastic-plastic stress fields at the crack tip are beyond the scope of the current work.

The crack growth directions are characterised in two ways: 1) as macroscopic crack growth directions (neglecting the microscopic changes), 2) as microscopic crack growth directions that can be matched with the individual directions of dislocation motion. These analyses are realised through high-resolution and high-magnification secondary

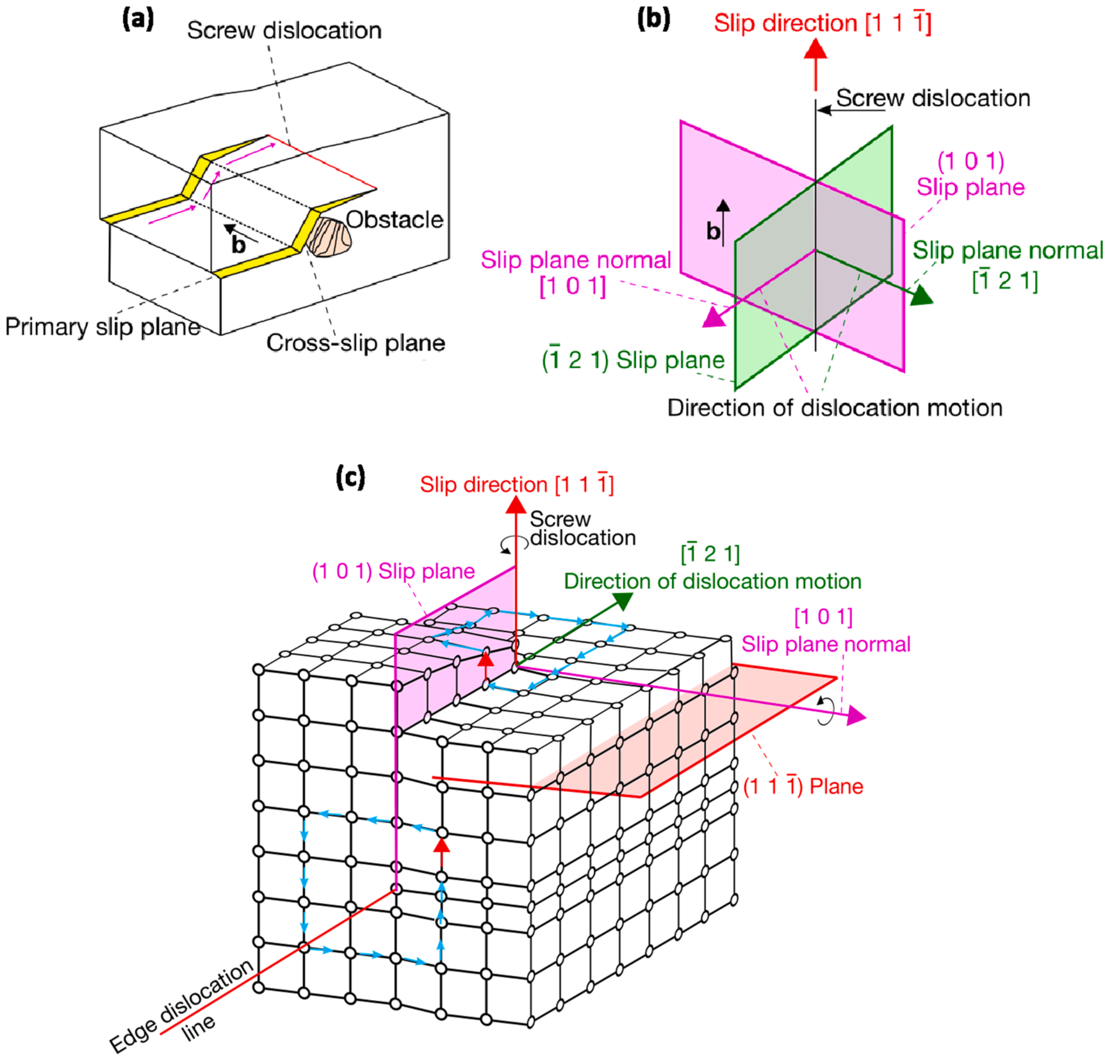

Fig. 2. Direction of dislocation motion (purple arrows) and cross-slip for a screw dislocation (a); dislocation motion directions for two selected orthogonal slip planes that share the $[11\overline{1}]$ slip direction (b), and the same represented for the crystal lattice, including rotations of the material around the slip direction and the specific slip plane normal (c). (For interpretation of the references to colour in this figure legend, the reader is referred to the web version of this article.)
Adapted from [57].

electron (SE) images. To analyse the crystallographic slip directions, the reference orientation of each grain is obtained using the clustering-based algorithm by Lehto [55], which detects the reference orientation by finding the most densely populated location in the orientation space for each grain. This is a good estimation since the orientation data is less dense in deformed regions because of the lattice curvature introduced by deformation.

3. Results

3.1. Fractography

Fracture surface analysis summarised in Fig. 3 focuses on pre-crack and crack front, while other fracture surface features (e.g. striation, persistent slip bands) are addressed in detail in [42]. The pre-crack zone highlighted in Fig. 3 differs clearly from the FCG zone. This is due to the different loading conditions between pre-cracking and fatigue test. The pre-crack zone shows a clear flat-like surface. Even though the pre-crack front is not strictly linear through the thickness, the picture confirms that a through pre-crack was achieved.

The fracture surface also does not show any evident sign of the so-called *tunneling*, i.e. when crack grows faster at the center of the sample, due to high stress triaxiality, and produces shear lips near the surface, usually at 45° from the maximum principal stress. These shear lips are driven by quasistatic damage modes and present the cup and cone feature, while the growing crack at the center produces deformation bands that nucleate voids in small particles. Crack tunneling would clearly affect both observations from DIC and FCG rate analyses. Fig. 3 clearly shows that these features are not identified on the fracture surface.

It is not uncommon, for the considered configuration, that different crack lengths would be detected on the two surfaces of the specimen due to unavoidable local microstructural differences [60]. However, despite asymmetries of the crack front, formation of faceted fracture surfaces close to the observed surface and as well as in the interior of the specimen are visible in the zone considered for the FCG rate analysis (i.e., until ≈0.4 mm). The fatigue crack propagates through the material forming a river pattern morphology, in the direction of microscopic crack path. Many parallel straight lines forming normal to the river pattern direction are observed on the fracture surface in the zone of interest as shown also in [42]. Based on Fig. 3 and on these observations, it is reasonable to assume that the behaviour of the fatigue crack propagation presented in later sections characterizes the near-surface and reasonably approximates the interior of the sample. In addition, the microstructure of the ferritic stainless steel considered here was extensively studied by the current authors in [42,45,61], which revealed that non-metallic inclusions (NMI) and plasticity induced crack closure did not play role in the following FCG rate observations.

3.2. Small crack behaviour and micromechanisms

Fig. 4 shows the FCG path, the grain boundaries (GB) and the accumulated shear strain localisation point (LP) detected by the DIC through the fatigue test. Further detailed analyses of the maximum shear strain localisation profile by DIC supported by the study of the fracture surface were presented in [42]. It was shown that the shear strain localisation is an area where shear deformation suddenly starts to increase steeply (i.e. “start of shear localisation”), and accumulates until a maximum value is reached; then it slows down (i.e. “stop of shear localisation”), and a subsequent localisation event takes place. This phase of a steep increment between the start and stop is called the “transitional stage”. The phenomena, therefore, happen at subsequent intervals of numbers of cycles, following each other. Outside this transitional stage of a steep increment, the accumulation of shear strain occurs at a lower rate, and it is mainly due to the crack opening. For the sake of clarity, the shear strain magnitude in Fig. 4b is the accumulated value detected at the end of the fatigue test, i.e. it includes all the accumulated shear strain induced by material cyclic deformation and crack opening. The shear strain magnitude at the end of the transitional stage (i.e. excluding the contribution due to crack opening) is reported in Table 1 for each LP. A total of five LPs were detected, located both inside the grains (LP 1, 2, 3, and 5) and at GB (LP 4). It should be noted

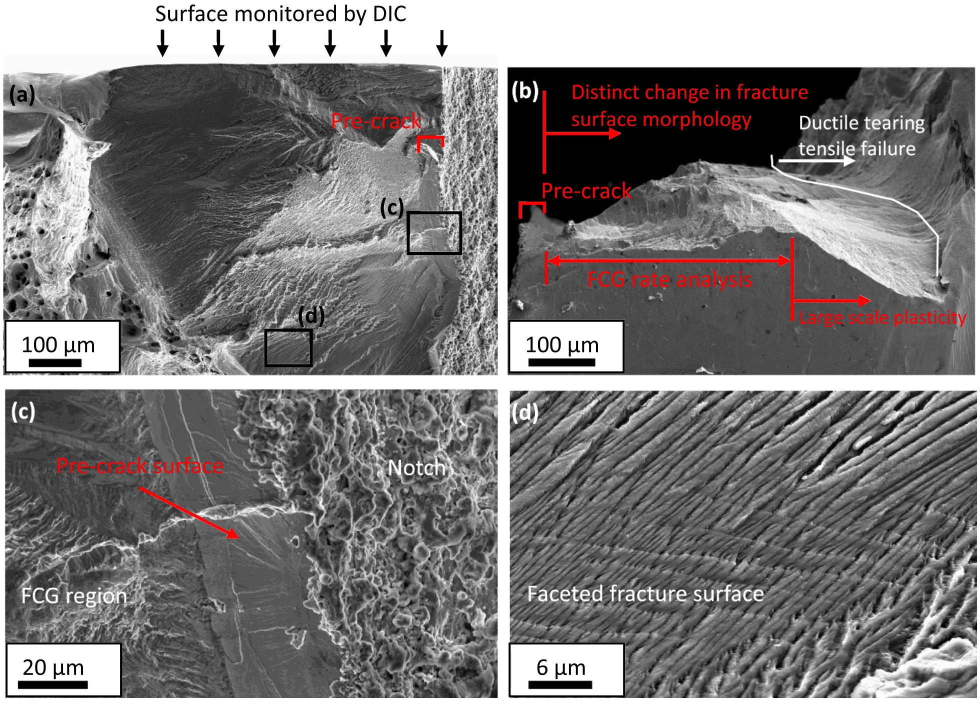

Fig. 3. Fracture surface of the considered sample, top view (a) and DIC side view (b); higher magnification of the pre-crack surface and FCG region near it (c); higher magnification of the faceted fracture surface of the interior of the specimen (d).

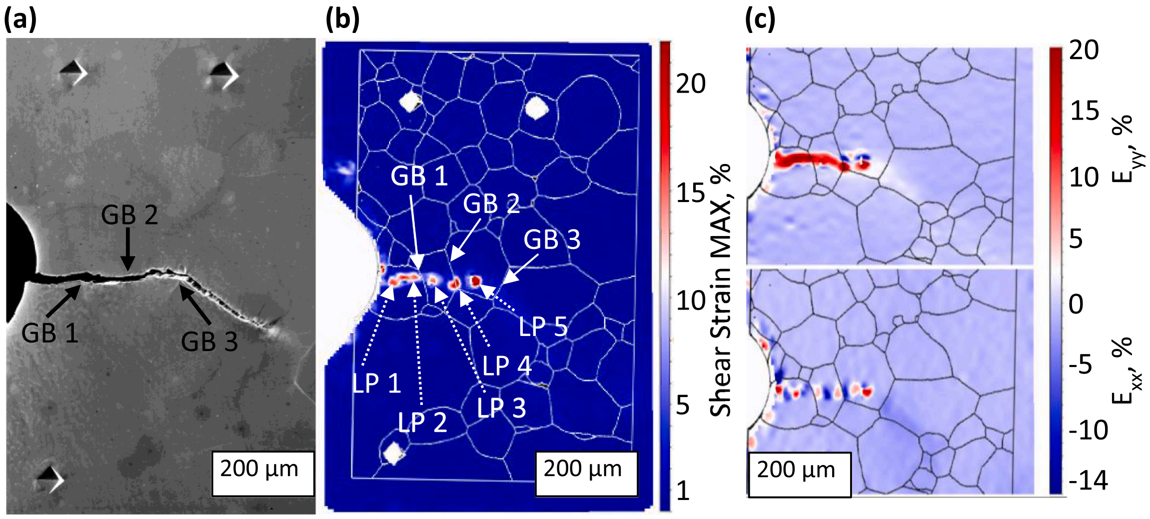

Fig. 4. SEM picture of the fatigue crack (a), summary of the max shear strain localisation point (LP) (b), and linear deformations E_{xx} and E_{yy} (c); note that the shear strain magnitude in (b) is the accumulated maximum value at the end of the fatigue test (i.e. because of the LP and crack opening), while the magnitude reached at the end of the transitional stage (stop) of the LP is reported in Table 1.

Table 1
Approximated values of the location of the shear localisation d (distance from notch root), distance Δ between the shear localisation and crack tip, corresponding number of cycles N at the start and stop of the shear localisation (transitional stage), and qualitative LP shear strain magnitude at the end of the transitional stage; see also insert in Fig. 5.

Strain localisation	d (mm)	N_{start}	N_{stop}	Δ_{start} (μm)	Δ_{stop} (μm)	Shear strain %
LP 1	0.077	32,001	45,007	13	≈0	3.5
LP 2	0.125	52,732	64,497	34	12	5.7
LP 3	0.183	68,808	90,802	65	18	9.3
LP 4	0.259	95,614	119,143	81	24	11.8
LP 5	0.308	121,413	143,153	69	24	14

that the strain localisation in between LP 1 and LP 2 is an extension of LP 2. Macroscopically, at an early stage the crack seems to propagate perpendicular to the direction of the applied load, while at the micro level clear alterations of the crack path are visible, as expected. A remarkable deviation of about 45° is shown towards the end of the test at $N \approx 162{,}500$ (where $N = 175{,}000$ is the total number of cycles before interruption of the test) when the crack crosses the last grain boundary of interest (GB 3). It must be emphasized that subsequent analyses and discussion are based on the crack growth data before this clear deviation occurs. During the propagation, the crack crosses three grain boundaries, in what seems mainly a transgranular-driven fracture.

The DIC analyses revealed several shear strain localisation events (LP) with an average maximum diameter of about 20–50 μm, i.e. the shear strain is highly localised at the grain level, while the macroscopic deformation is still small. The size and shape of the LP are an approximative estimation since precise quantification is not yet possible from DIC analyses. These events occurred along the path of the crack but always ahead of it. This aspect is better underlined in Fig. 5, where the crack stemming from the notch, l, and the distance of the LP from the notch root, d, are plotted as a function of the number of cycles, N. The start of the strain localisation events, marked as blue cross, always takes place ahead of the crack tip at the distance Δ.

Still referring to Fig. 5, the local data variation of the experimental small fatigue crack lengths l is smoothed by the incremental polynomial regression. At the crack lengths of 0.16 mm, 0.26 mm, and 0.41 mm the crack crosses the grain boundaries, while at 0.41 mm it makes a clear deviation of 45° from its original path. As mentioned before, strain localisation analyses consider the crack growth data before this clear deviation occurs. The shear strain localisation always starts ahead of the crack tip. During the transitional stage, i.e. the steep increment of shear deformation inside the LP [42], the crack advances towards the localisation. When the crack tip reaches the LP, the transitional stage stops, and a new and subsequent localisation event takes place ahead of the crack tip, repeating the same process. The distance Δ between the crack tip and LP therefore has a maximum value at the start of the shear localisation, and a minimum value when the shear localisation stops. This distance is different for each LP, but always in the range of 0–90 μm (see Table 1). It should be noted that strain localisation may start in the subsequent grain while the crack tip is still behind the grain boundary. By referring to Fig. 5, this is the case for LP 3, for example, which starts after GB 1, in the second grain, when the crack tip has not yet crossed GB 1 and is still propagating in the first grain. The same observation applies to LP 5. For the sake of clarity, the values of Δ, d, and the corresponding cycles N at the start and stop of the shear localisation are summarised in Table 1, together with approximate values of the shear strain localisation when the process stops (see also [42]).

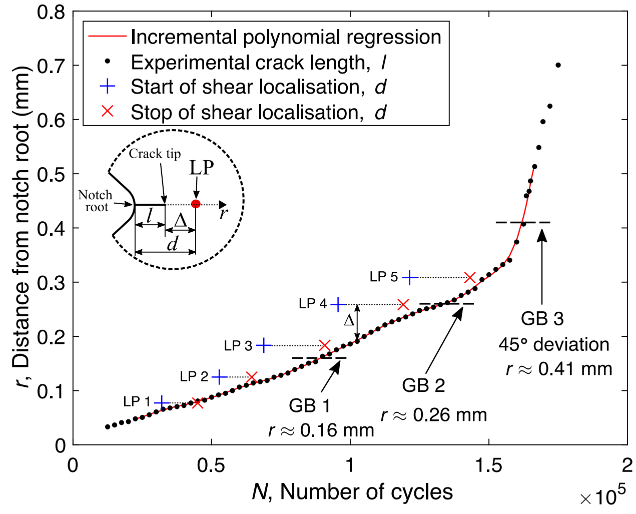

Fig. 5. Small fatigue crack length l (stemming from the notch) and location d of the shear localisation point (LP, start and stop), versus the number of cycles N; for a given LP, its distance from the crack tip is reported as Δ; until GB 3, the crack is growing macroscopically perpendicular to the direction of applied load.

Fig. 6 shows the small FCG rate evaluated using the crack lengths generated by the local polynomial regression of Eq. (1) and, only for comparison, the FCG from direct secant calculation. Since $n = 4$ in the local polynomial regression, the first and last four crack lengths l of Fig. 5 do not have a corresponding FCG rate value in Fig. 6. For the sake of consistency, these first and last four points have also been excluded from the plot of the direct secant calculation. The incremental polynomial regression reveals the oscillatory behaviour of the FCG rate, composed of several peaks and valleys, while the direct secant calculation does not permit to reveal such trend due to the small crack increment related measurement limitations mentioned in Section 2.2. For the sake of clarity, further considerations and analyses always consider the FCG rate evaluated by the incremental polynomial regression. The same figure also shows when a grain boundary is crossed, or a shear strain localisation occurs in relation to those peaks and valleys. Before further discussion, it should be noted that Fig. 6a shows how the FCG rate behaves with highlights on when an LP transitional stage occurs, but without explicit information on the relative location of LP. Therefore, one should not seek to directly reflect Figs. 6a and 4b in the spatial domain. Let us consider an example: LP 5 is clearly located in the middle of grain 3, in between GB 2 and GB 3, as correctly depicted in Fig. 4b. However, Fig. 6a shows that LP 5 starts when the crack tip has yet to cross GB 2, and then stops when the crack tip is in proximity to LP 5, after crossing GB 2. Fig. 6a highlights exactly this period of time during which an LP is developing, and the related FCG rate is enclosed in the shaded areas. To this regard, an explanatory video is provided in the supplementary material (see Appendix B) to better illustrate crack growth evolution and the relation between these figures. The proper location of LP, and therefore how the FCG rate behaves when the crack tip is physically crossing the LP location, is depicted in Fig. 6b. By keeping these considerations in mind, Fig. 6 shows that, interestingly, grain boundaries can be found both at peaks and in valleys, with no evident direct correlation with the FCG rate. However, they seem to affect how the FCG rate and strain localisation interact. At first glance, crack retardation seems to be correlated with strain localisation events since an evident alteration of the FCG rate mainly occurs during the strain accumulation process (shaded area in Fig. 6a) or when the crack physically crosses an LP (Fig. 6b). In the discussion section, the FCG rate and each LP will be further addressed and reflected on holistically in the light of microstructural deformation and damage analyses. It will be revealed: 1) why LP 3 and LP 4 in Fig. 6a do not show a clear FCG rate alteration during the strain accumulation process, 2) why the FCG rate retardations in Fig. 6b occur when the crack crosses an LP, and 3) why the retardations have different magnitudes.

Concluding, some differences in the FCG rate curve are found between Fig. 6 and our earlier study in [42], mainly because of the higher number of data points in the present work and the constant interval at which these are evaluated. This highlights the importance of a high sample rate when the polynomial regression-based FCG rate calculation is used.

3.3. *Microstructural analysis*

3.3.1. *Grain structure and deformation caused by cyclic loading*

The mechanisms of crack growth are studied through a detailed EBSD deformation analysis. Fig. 7 compares the area monitored by DIC before (a, d) and after (b, e) the fatigue test, and the nickel-plated subsurface section (c, f). The top row shows the as-measured orientation maps (IPF-X) and the grain reference orientation unit cells overlaid on SE images. The crack growth analysis was realised within the first three grains which are visible in all cross-sections of Fig. 7a-c. For further reference, the grains are referred to as g1, g2 and g3, correspondingly. While there are apparent morphological differences in the grain structure, 24 out of 29 grains in the nickel-plated dataset (Fig. 7c) can be identified with grains visible in the other datasets (Fig. 7a,b). The plane of observation for the nickel-plated specimen is approximately 56 ± 7 μm below the original specimen surface. This value is determined by comparing the size of the grains in the nickel-plated dataset to the size measured before the fatigue test. To this end, a spherical grain shape is assumed, and the Pythagorean theorem is applied to the measured circle equivalent radiuses.

The domain misorientation analysis in Fig. 7d reveals a degree of deformation on the sample surface prior to the fatigue testing, in the form of near-horizontal lines. However, the magnitude is quite small, and the domain misorientation in Fig. 7d shows a relatively even deformation state. After the fatigue test, considerable deformation is visible within the grains; see Fig. 7e. In the early phases of crack growth within the first two grains g1 and g2 the changes are quite small, with progressively larger deformation observed as the crack length increases. In the third grain g3 there is already considerable deformation, and the black dashed lines show the approximate area of deformation over the entire fatigue crack. Fig. 7c shows that the crack morphology in the nickel-plated section partially differs from the surface section, while the general directions agree with those depicted in Fig. 7b. The domain

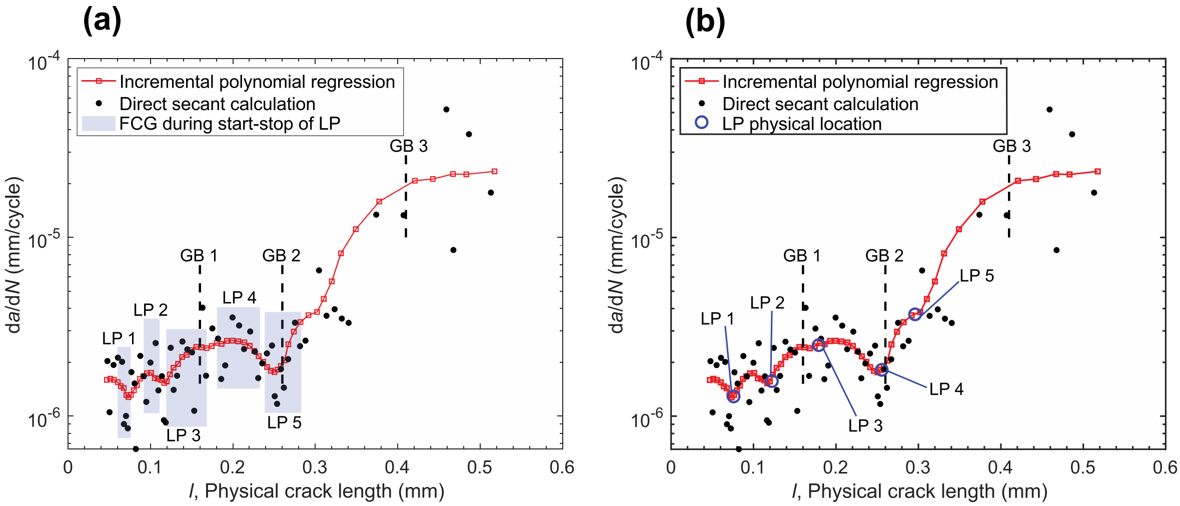

Fig. 6. Comparison of the fatigue crack growth rate of a microstructurally small fatigue crack evaluated by the incremental polynomial regression and the direct secant calculation of the raw experimental crack lengths; (a) FCG during the transitional stage (i.e. start-stop) of the LP and (b) FCG at the physical location of the LP; the pictures also report when a grain boundary (GB) is crossed; log-log scale; until GB 3, the crack is growing macroscopically perpendicular to the direction of applied load; see also supplementary material (Appendix B).

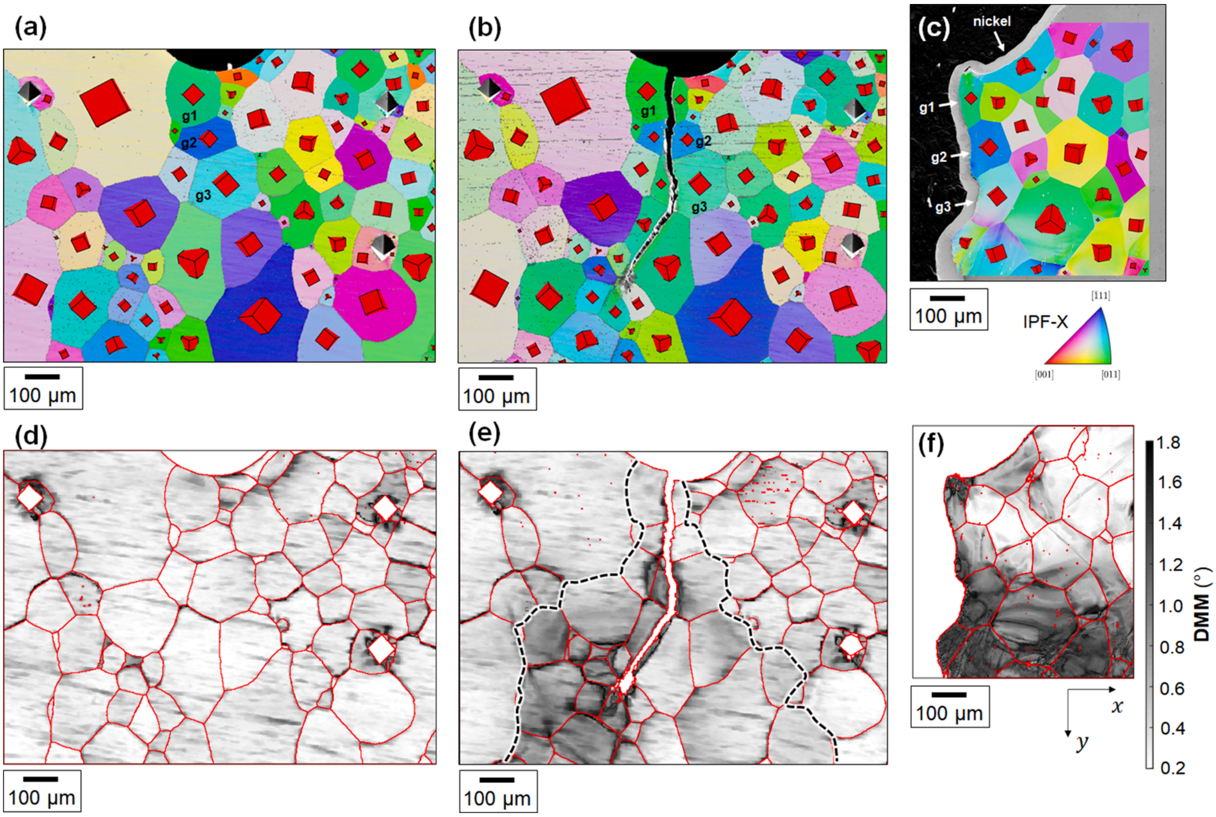

Fig. 7. As-measured orientation maps (IPF-X) and grain reference orientation unit cells overlaid on secondary electron images for the samples before testing (a), after fatigue test (b), and for the nickel-plated section (c); domain median misorientation (DMM, $\Delta\theta = 2^\circ$, kernel size 150 × 150 µm within step size accuracy) for the three samples showing the general extent of deformation in the samples (d-f).

misorientation analysis in Fig. 7f shows that deformation increases progressively through grains g1, g2 and g3. A similar outline of deformation can be identified, although the magnitude of deformation seems to be higher compared to Fig. 7e. Next, more detailed analyses will be carried out to characterize the size of the deformation induced grain substructures along the fatigue crack.

3.3.2. *Spatial size distribution of grain sub-structures*

The heterogeneity of microstructural deformation is studied through the spatial size distribution of dislocation cells and sub-grains in Fig. 8. In general, the surface section in Fig. 8a,c shows less sub-structures near the crack face compared to the sub-surface section in Fig. 8b,d. The substructures on the surface section may be partially hidden by the deformation observed on the sample surface (Fig. 7d). Still, the dislocation cell size in Fig. 8a shows an intermittent appearance especially within grains g1 and g2. For the sub-surface section in Fig. 8b, the size of the dislocation cell decreases as the crack length increases, and the extent to which they cover the grains also increases. The exception is the crack initiation location, where dislocation cells smaller than 5 µm cover the top part of grain g1. Next to the crack face this zone extends to 25 µm from the notch, with the elliptical shape extending up to 50 µm below the notch. This is likely caused by a secondary crack (see following analysis), and by the stress concentration effect of the notch. Similarly sized small dislocation cells have also formed in grain g3 near the crack face. The deformation layer induced by EDM is also found to be negligible, with an observed thickness of approximately 10 µm. The dislocation cell size contours in Fig. 8b indicate a higher amount of dislocation cell formation towards the lower half of the grains, especially in grains g2 and g3. Sub-grain formation appears to be limited to the vicinity of the crack face for both sections of observation; see Fig. 8c,d. For the sub-surface section, a refined sub-grain structure has also formed near the notch. Along the path of the fatigue crack an intermittent appearance of the sub-grain size is observed in the lower half of grain g2 and in the entire grain g3. Next, the microstructural deformation patterns and crack growth directions will be investigated in detail.

3.3.3. *Deformation pattern and crack growth direction analysis*

The fine dislocation cell structure and analysis of the macroscopic crack growth direction are shown in Fig. 9. The high-resolution SE image (Fig. 9b) reveals that a secondary crack 12 µm in length was arrested in grain g1. This explains the deformation field and large number of fine dislocation cells at the top of grain g1, indicating the plastic deformation zone at the tip of the secondary crack. This result, supported by the comments on Fig. 8, suggests that the plastic contribution due to the notch effect fades quickly and it is limited to the very top end of g1. Given the size of the pre-crack ($\approx$20 µm), the FCG rate analysis begins from a crack length of $\approx$48–50 µm which is already outside the highly deformed zone of g1. Thus, the notch effect is negligible.

In terms of microstructural deformation patterns, the size of the dislocation cells is similar on both sides of the grain boundary GB 1, but the heavily deformed region is approximately three times wider in g1 (Fig. 9a). At GB 2 such behaviour is not observed, with the size of the dislocation cells and deformation zone being similar in grains g2 and g3. The gradient of the dislocation cell size is strongest in grain g3, with the smallest sizes being observed at the bottom of the grain adjacent to GB 3, and extending much further along the GB in the horizontal direction (x+) compared to grains g1 and g2. In general, lattice curvature is also observed, shown as grayscale gradients without distinct deformation patterns.

The macroscopic crack growth directions are analysed in Fig. 9b to find correspondence with the expected dislocation motion directions for screw dislocations. Here, the $\langle 11\overline{1}\rangle$ slip direction with the following criteria is displayed: 1) highest or near-highest individual Schmid factor, and 2) multiple slip planes with high Schmid factors. The cyan-magenta

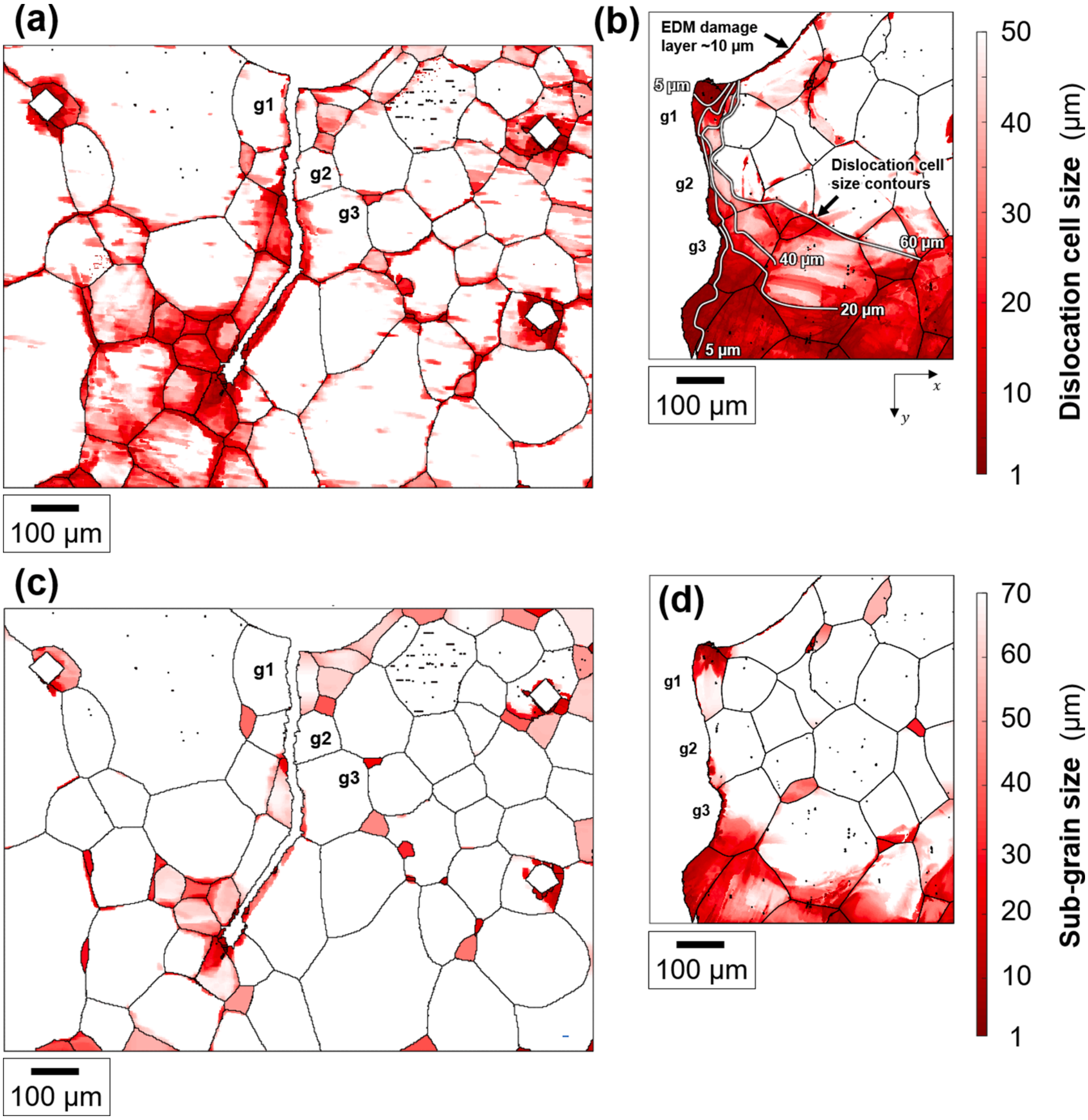

Fig. 8. Spatial size distribution for dislocation cells (a, b) and sub-grains (c, d). The white contours with µm values in (b) indicate the dislocation cell size. The analysis is shown for the specimen after fatigue, step size = 2 µm (a, c), and the nickel-plated specimen, step size = 0.5 µm (b, d). (DMM, $\Delta\theta = 0.5^\circ/\Delta\theta = 2^\circ$, kernel size 150 × 150 µm within step size accuracy).

colour scale indicates the Schmid factor of each slip system, while the directions for dislocation motion on {110} and {211} slip planes are indicated by purple and green segments, respectively. The macroscopic crack growth direction is quite constant in grain g1, with the change in direction at any given point being subtle. In comparison, the macroscopic crack growth direction has multiple sharp deflections in grains g2 and g3, with the deflection angle sometimes exceeding 90°.

While the dominant macroscopic crack growth directions follow the {211} slip planes, it is possible that on a microscopic scale deformation is taking place in the {110} slip planes. For this reason, the crack growth directions are analysed in more detail for grain g3 showing the above-mentioned characteristic. As shown in Fig. 10a, the majority of macroscopic crack growth directions between segments 1–9 show good correspondence with the dislocation motion directions of the $(11\bar{2})[111]$ slip system, with agreement observed to other {211}[111] and {110}[111] slip systems of Fig. 10c as well. On closer inspection, the microscopic crack growth directions shown in Fig. 10b show agreement with multiple {211} and {110} slip planes.

4. Discussion

The interaction among the crack tip and surrounding local phenomena is clearly very intricate. The current work brought out two factors in particular: the shear strain localisation (occurring ahead of the crack tip) and microstructural features (e.g. grain boundaries, microstructural deformation). Fig. 6 shows that proximity to an LP results in a FCG rate retardation [37,62], followed by acceleration once the LP is crossed. Two phenomena have influence, namely 1) the transitional stage (Fig. 6a), and 2) the physical location of the LP (Fig. 6b). The latter acts as a physical barrier that must be bypassed by the crack tip to enable further crack growth, and all FCG rate retardations are clearly located at LPs, though of different magnitudes, as will be discussed later. With respect to Fig. 6a, i.e. with a focus on the role played by the transitional stage, the crack retardation seems to begin when the LP starts to form at the distance Δ from the crack tip. While this observation is clear for LP 1, LP 2, and LP 5, which all have a valley (i.e. a low FCG rate value) located in the shaded area depicted in Fig. 6a, some exceptions occur for LP 3 and LP 4. This can be explained by the fact that when LP 3 starts to form, the crack tip is in the first grain, while LP 3 is in the second grain (see

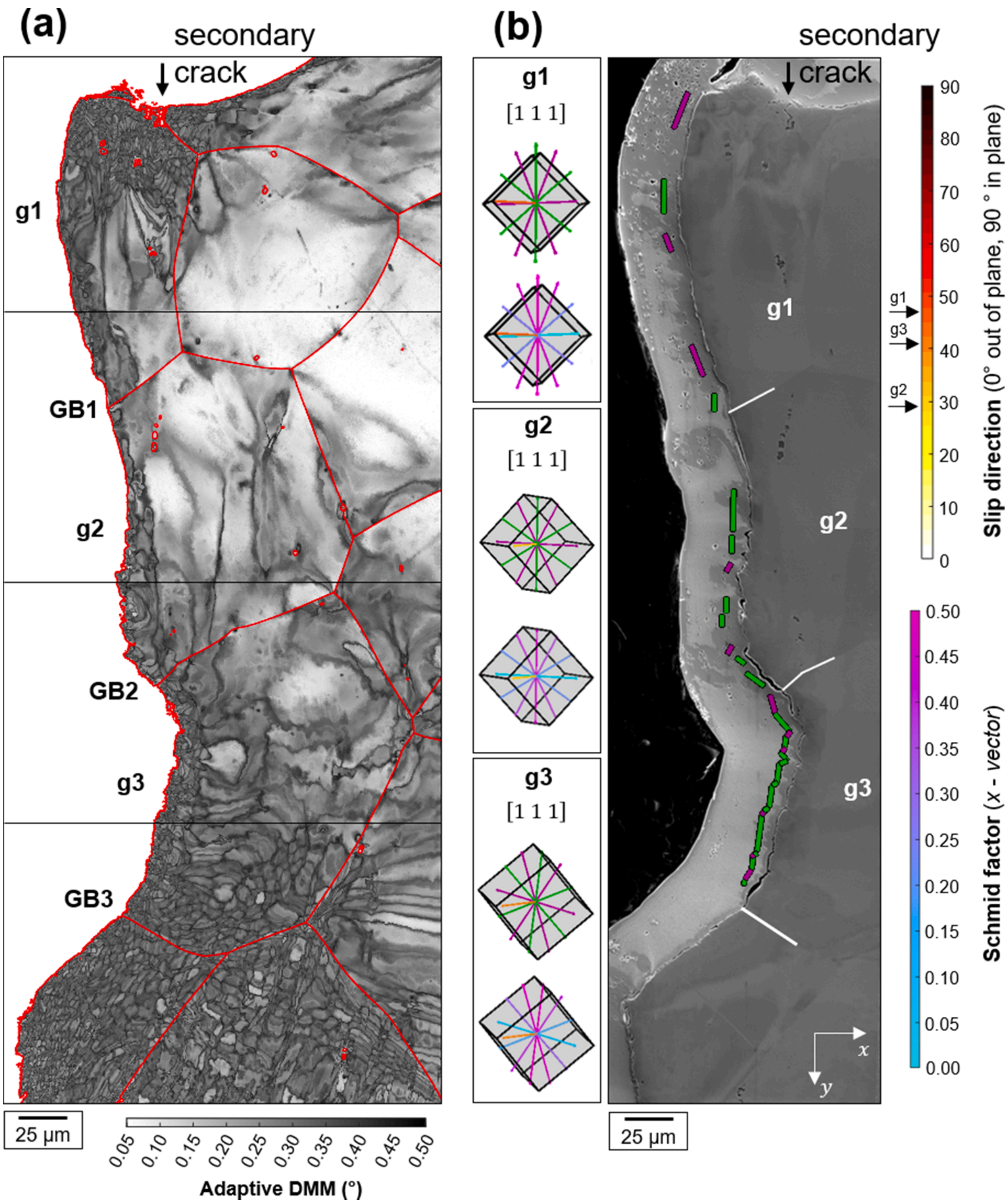

Fig. 9. Dislocation sub-structure and crack growth analysis for grains g1-g3. Adaptive domain misorientation showing the fine dislocation cells, step size 0.1 μm, $\Delta\theta = 0.5°$, kernel size 24.1 × 24.1 μm (a); image combined from several high-magnification SE images (flat position), and the directions of dislocation motion for the slip direction with the highest Schmid factors for each grain, with traces showing agreement with the macroscopic crack growth directions (c); trace colours: purple-{1 1 0} planes, green-{2 1 1} planes. (For interpretation of the references to colour in this figure legend, the reader is referred to the web version of this article.)

Fig. 5 for relative location) at a relatively large distance Δ from the crack tip (Table 1). GB 1 seems to act as a shield (obstacle to dislocation motion [37]) for crack tip - LP interaction, and indeed, a small reduction in the FCG rate can only be observed right after crossing GB 1, which until that moment did not directly affect the crack growth. Fig. 6b shows that this small reduction of the FCG rate occurs when the crack tip physically penetrates LP 3. At this stage, LP 4 takes place. At the beginning, the crack tip does not have a clear obstacle to grow through, given that LP 4 is located approximately at GB 2, at the largest distance Δ from the crack tip (Table 1, Fig. 5 for proper relative location). The FCG rate increases slightly, and then starts to decrease only when the crack tip is relatively close to LP 4. It can be inferred that the shielding of the crack tip - LP interaction is only partial in this case, because of the slightly more favourable location compared to LP 3. When the crack tip has propagated beyond the physical location of LP 4, the FCG rate starts to continuously increase, and GB 2 does not seem to act as a physical barrier. However, given that LP 4 is located approximately at GB 2, it is difficult in this case to definitively exclude any role of the grain boundary. The subsequent reduction of the FCG rate occurs only when the crack tip is penetrating LP 5 (see Fig. 6b), while GB 3 does not have any further influence. However, our findings do not mean that the GBs do not play any role at all, but rather that in some cases they do not act as physical barriers. Strain localisation, indeed, is still a consequence of local inhomogeneous microstructure, including GBs. Lastly, it should be noted that neither the shape nor the size of the LP can be accurately quantified and therefore considered in Fig. 6b. This would most

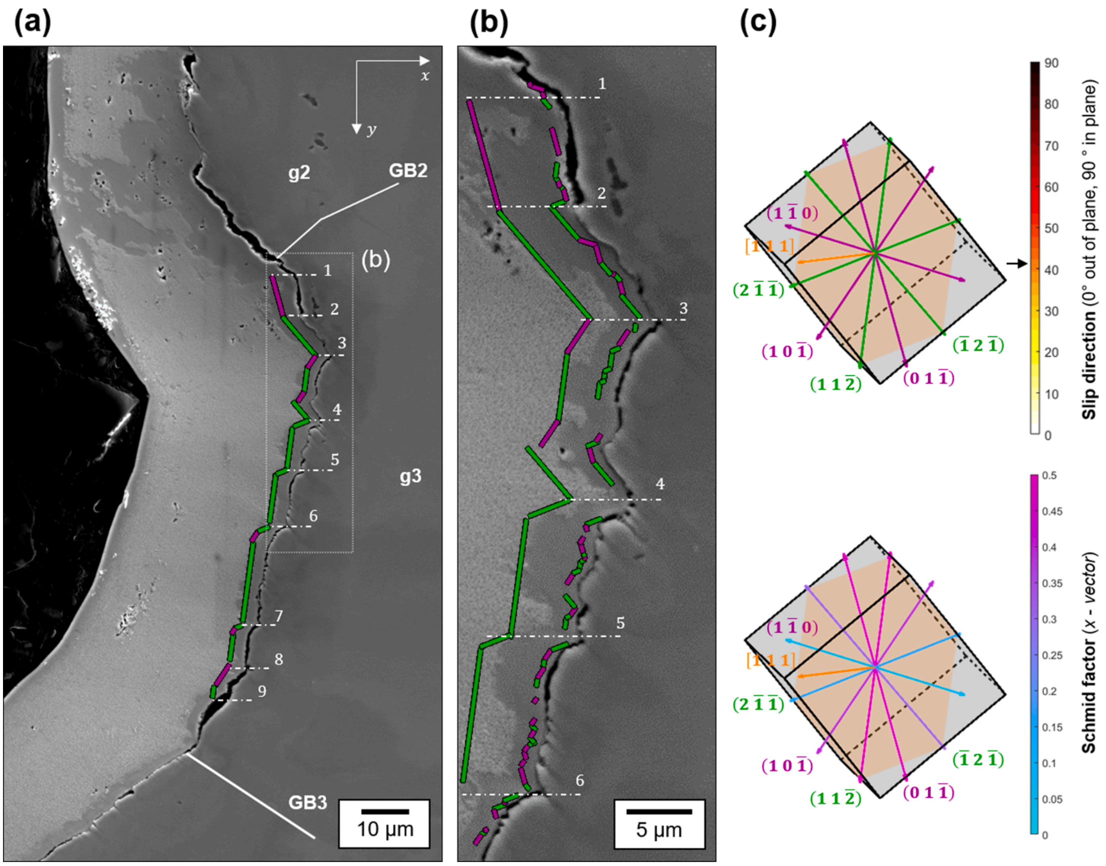

Fig. 10. Crack growth direction analysis for the nickel-plated dataset and grain g3. The macroscopic crack growth direction changes between segments 1 and 9 (a); comparison of macroscopic and microscopic crack growth directions between segments 1 and 6, the traces are shifted only in the horizontal direction (b); directions of dislocation motion and Schmid factors for the [1 1 1] slip direction (c).

probably further improve the correlation between the physical location of LPs and the lowest FCG rate zones, allowing for a proper positioning of the former.

These features, despite being distinctive, are also in line with the observations of other authors. Rovinelli at al. [17] performed a sophisticated analysis of small crack propagation by combining in situ high-resolution 4D experiments, machine learning, and crystal plasticity simulations. The authors revealed a strong correlation between the maximum accumulated plastic shear strain, crack length, and crack growth rate, while grain boundaries showed a very low correlation. A clear retardation effect resulting from strain localisation was also reported by Matsushita et al. [23]. Our observations also agree well with the results of Newman [63], and the early works of Pearson [64] and Lankford [65], which do not exhibit a physical barrier effect at the grain boundary for the growth rate of small fatigue cracks. Other studies in the recent literature have instead shown how GBs may directly affect the crack growth (see e.g. [66–69]). Most notable the model proposed by Zhai et al. [68] based on slip geometry explains how misorientation affects the propagation of cracks across the GBs. On the other hand, Hansson et al. [70] demonstrated that high-angle grain boundaries do not affect directly the FCG rate, while low-angle boundaries can result in both retardations and accelerations of FCG rate, or have no effect at all. Discrete dislocation mechanism, however, does not consider the possible formation (and role) of strain localisations. Moreover, fluctuations in the FCG rate have been observed in single crystal materials [71]. Analyses of grain boundary misorientation and resistance plotted in Fig. 11 show that misorientation angles do not correlate with strain localisations and retardations in current study. The factor *m'* represents the co-planarity of incoming and outgoing slip-systems, with 1-*m'* indicating the resistance of the GB for slip transmission [72]. The highest resistance is found

	Misorientation		GB resistance
	Angle (°)	Axis [xyz]	1 - m'
GB1	20.7	[-0.30, 0.95, -0.01]	0.10
GB2	17.4	[-0.61, -0.68, -0.42]	0.07
GB3	43.4	[0.10, 0.96, -0.22]	0.28

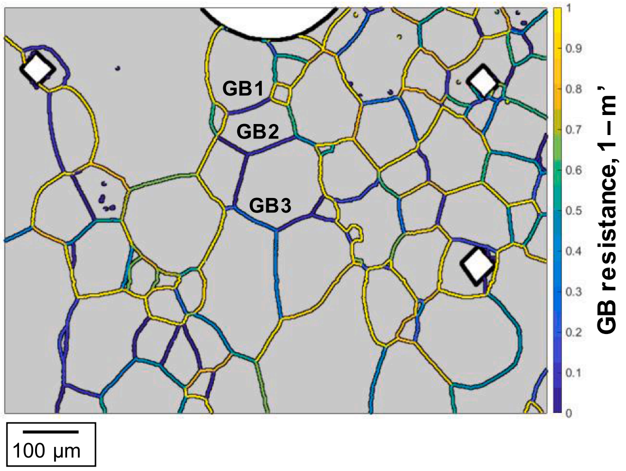

Fig. 11. Grain boundary misorientations and GB resistances based on co-planarity of slip systems, with 1-*m'* ranging from 0 (transparent GB) to 1 (impenetrable GB). The {1 1 0}[1 1 1] slip system with the highest Schmid factor (Fig. 9) is utilized for the crack growth area, while elsewhere the {1 1 0} ⟨1 1 1⟩ slip system with highest individual Schmid factor is assumed.

for GB 3, which instead shows the most negligible influence on the FCG rate. The GB 2 has the lowest resistance and misorientation angle, but interestingly LP 4 and the largest FCG rate retardation occur in its proximity (see Fig. 6b). It can be concluded that the major part of retardation events can be associated with the shear strain localisation, which is still a consequence of local inhomogeneous microstructure. Therefore, investigation of microstructural deformation mechanisms is needed to deepen the understanding of the interaction between crack growth and microstructural features. Analysis of microstructural deformation mechanisms is also necessary to clarify why the retardations occur at LPs and are of different magnitude.

With respect to the role played by the physical location of LP (see Fig. 6b), the reduction in the FCG rate when the crack tip is crossing LP 3 or LP 5 is relatively small if compared with other strain localisation events. The macroscopic crack growth direction analyses revealed that intense macroscopic cross-slip occurred in the grains (see grains g2 and g3 in Fig. 9 and Fig. 10). Both grains g2 (LP 3) and g3 (LP 5) have many slip systems with similar high Schmid factors. This mechanism most probably facilitates the crack in avoiding and going around the strain localisation damaged zone [73], and therefore the retardation effect on the FCG rate is minimised. For the LP where FCG rate retardation is more pronounced, the crack tip penetrates the local LP zone to some extent. Carroll et al. [37] also observed that while strain accumulation may have contributed to retardation, strains associated with crystallographic slip may have created conditions favourable to faster crack growth and, more importantly, may have affected the crack path.

The hypothesis is further confirmed in Fig. 12, where the maximum shear strain during the fatigue test is overlaid on the SE image, and the size of grain sub-structures is shown. The crack propagates macroscopically in approximately the same direction until LP 1; at this point the

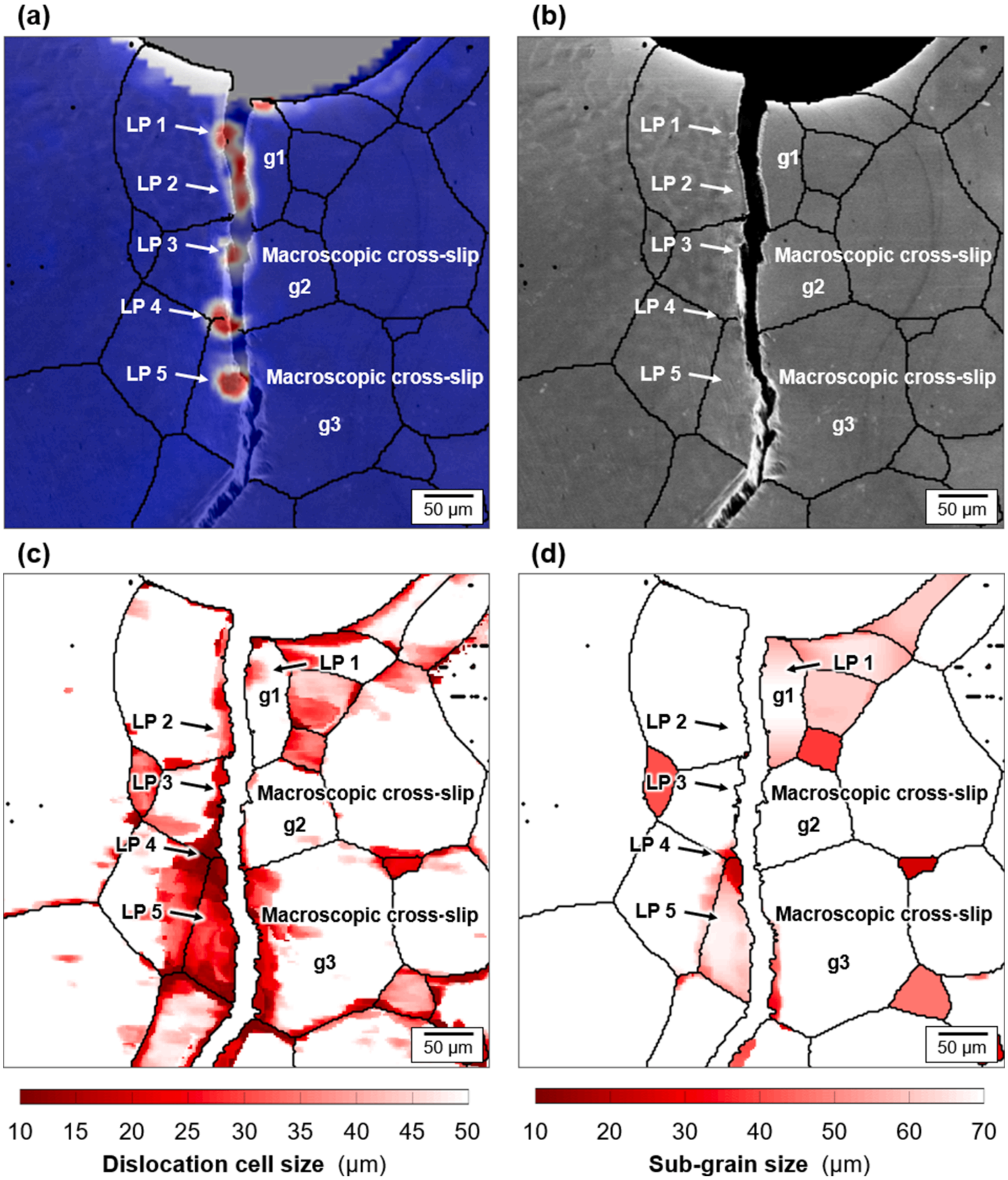

Fig. 12. Maximum shear strain during crack growth overlaid onto a secondary electron image taken in the EBSD configuration (a); secondary electron image (b); dislocation cell size ($\Delta\theta = 0.5^\circ$) (c); sub-grain size ($\Delta\theta = 2^\circ$). For all images high-angle grain boundaries are overlaid with the colour black, and the zones with the most pronounced macroscopic cross-slip (LP 3 and LP 5) are highlighted by notation. Step size 2 µm, kernel size 150 × 150 µm within step size accuracy.

crack growth direction has only a few small alterations, after which it settles into a new direction. The influence of LP 2 and LP 4 is even less pronounced, with only a minor deviation in growth direction taking place. The crack seems therefore to penetrate through LP 1, LP 2, and LP 4. The retardation of FCG rate is the most pronounced at LP 4, and this location shows the largest area of small dislocation cell and sub-grain sizes; see Fig. 12c,d. Areas of small dislocation cell size are also observed for LP 1 and LP 2, albeit the degree of refinement is smaller, and covers a smaller area. The formation of small grain sub-structures indicates accommodation of plastic strain at the microstructural level, which leads to local hardening of the material [24,34].

Significant disturbances in the macroscopic crack growth direction are observed at LP 3 and LP 5. The locations where the crack growth direction changes occur also exhibit intermittent areas of small dislocation cell and sub-grain in grains g2 and g3, as shown in Fig. 12c,d. A detailed analysis of grain g3 (i.e. LP 5) is shown in Fig. 13. Intermittent microstructural deformation patterns are located where the direction of the crack changes. In these cases, the crack seems to go around and partially avoid the physical location of the LPs, and thus the influence on the FCG rate is relatively small despite the microstructural deformation and the consequent material hardening. Next, we discuss the changes in crack growth direction from the perspective of microstructural deformation mechanisms.

Overall, the most pronounced macroscopic cross-slip steps are observed in grain g3, both on the surface of the specimen (Fig. 13a), and sub-surface (Fig. 10). The macroscopic growth directions for the sub-surface section are overlaid on the microstructural deformation patterns in Fig. 14. The heterogeneous deformation patterns are evident from the dislocation cell size (Fig. 14a) and especially the sub-grain size (Fig. 14b). Particularly at segments 4 and 5 it seems that the crack has gone around the hardened material regions. The crack path tightly wraps the semi-circular deformation patterns, and the direction changes occur when entering the next semi-circular feature. Microscopically the crack growth directions were shown in Fig. 9 and Fig. 10 to be mostly aligned with the slip plane that has the highest resolved shear stress according to the Schmid factor, either with the {110} or {211} slip planes. While macroscopically a large part of the crack growth could be identified with a {211} type slip plane in grain g3, closer inspection in Fig. 10 shows that cross-slip is taking place mostly in the {110} slip systems. Even on a microscopic scale, some segments were still aligned with the {211} slip plane directions, indicating elementary cross-slip in the neighbouring {110} planes. These observations are consistent with the work of Marichal et al. [57], who reported that {110} slip in equal elementary steps produces macroscopic {211} traces, or an arbitrary direction when the steps are non-equal. In our study some segments could not be associated with a crystallographic direction, which can possibly be explained by cross-slip in non-equal steps in the neighbouring {110} slip planes.

The main findings of the current experimental investigation reveal some fundamental aspects that should be carefully reflected in analytical models. The results show that the role of microstructure in the propagation of small fatigue cracks cannot be reduced only to the GB effects. This finding is particularly relevant since several modifications of LEFM have been proposed to consider the microstructural effects, such as grain orientation and microstructural barriers; see e.g. [12,74–78]. Usually, the microstructural length for modelling is defined on the basis of microstructural features observed only before the fatigue process, such as grain boundaries and metallurgical obstacles. However, it is clear from the results that the microstructural evolution is also important. Crystal plasticity models could describe the grain behaviour and the effect of grain interaction, but significant development is still needed to model the hundreds of thousands of load cycles (high cycle fatigue regime) required to create a physical accumulated shear strain localisation and grain sub-structures. Alternative approaches could make use of non-local damage models to describe the averaged FCG rate within a microstructure-related continuum unit [77,79,80]. However, the definition of the microstructure-related homogenisation unit and formulation of non-local damage models, especially for microstructurally small fatigue cracks in a high-cycle fatigue regime, still require future work. The main challenge is how to incorporate these microstructural factors into a realistic fatigue model suitable also for large and complex engineering structures and components. In general, once the most important local phenomena involved in small FCG and their correlations are revealed, the identification of a relevant small fatigue crack driving force should be possible (see e.g. [81]). This driving force could then be generalised towards a parameter representative of microstructural features, and finally incorporated into fatigue models of engineering relevance, e.g. microstructure and strain-based fatigue life approach.

5. Conclusions

From the current work, it emerges that for microstructurally small fatigue cracks, it is not a single factor that influences the FCG rate and the crack path, but rather the interaction of several elements developing during the fatigue process across multiple length scales, such as the accumulated local shear strain, microstructural deformation patterns, and crack path and length. The results show that shear strain localisations occurring ahead of the crack tip affect the FCG rate in coarse-

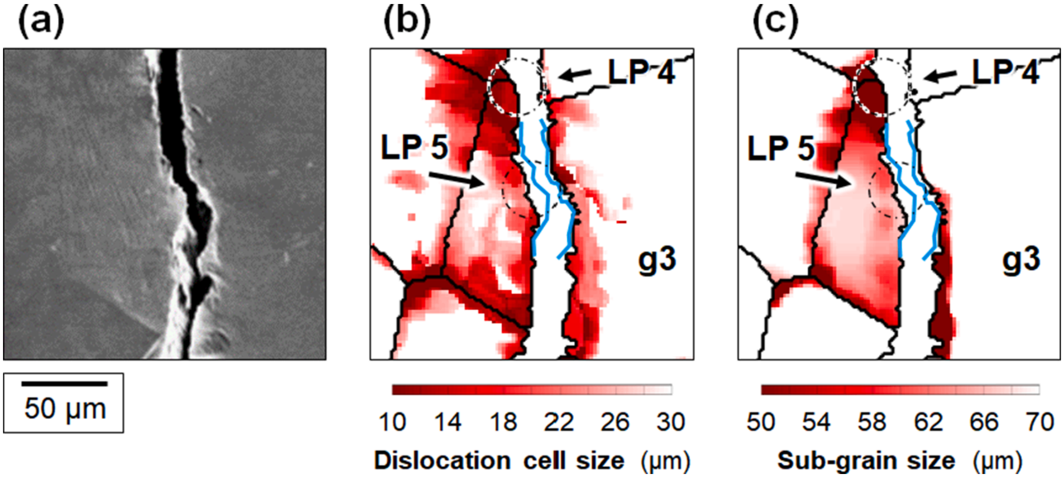

Fig. 13. Close-up of the macroscopic slip steps in g3 (a); spatial variation of dislocation cell size ($\Delta\theta = 0.5^{\circ}$) (b); spatial variation of sub-grain size ($\Delta\theta = 2^{\circ}$) (c). The crack path from (a) is overlaid with the blue lines in (b) and (c); the dash-dotted circles show the strain localisations LP 4 and LP 5 from DIC analyses. Step size 2 μm, kernel size 150 × 150 μm. (For interpretation of the references to colour in this figure legend, the reader is referred to the web version of this article.)

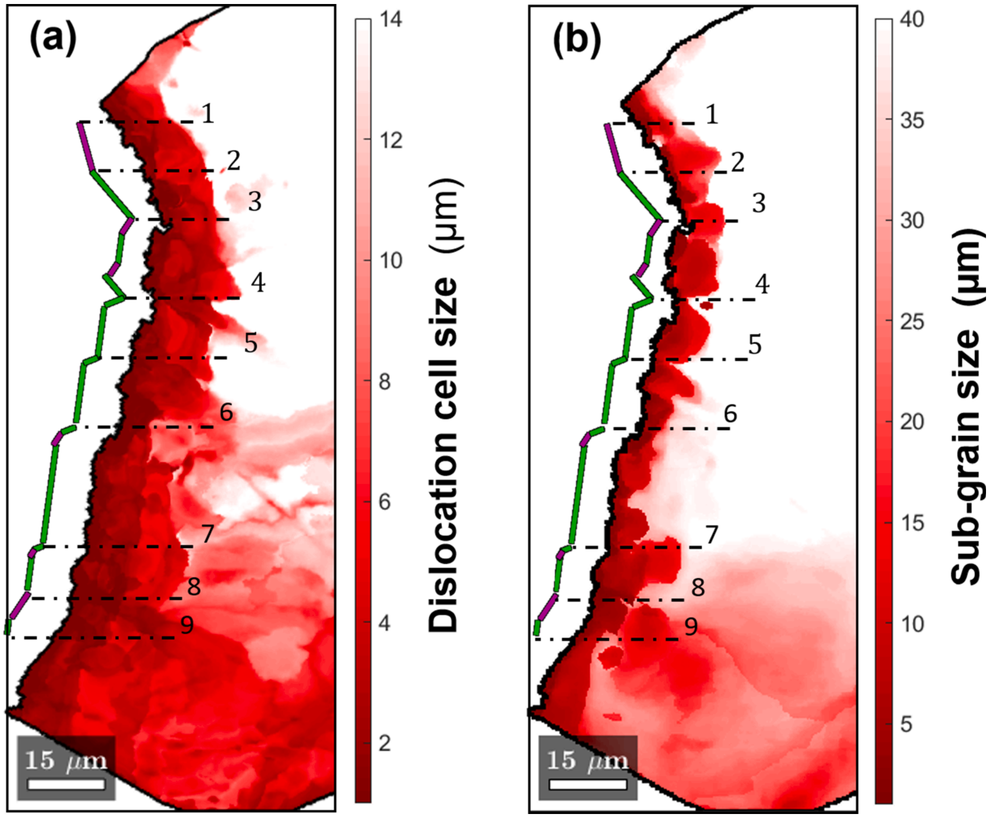

Fig 14. Close-up of the microstructural deformation patterns for the grain g3 for in the nickel-plated section, with macroscopic slip directions overlaid from Fig. 10; spatial variation of dislocation cell size ($\Delta\theta = 0.5^{\circ}$) (a); spatial variation of sub-grain size ($\Delta\theta = 2^{\circ}$) (b). Step size 0.2 μm, kernel size 96.2 × 96.2 μm.

grained BCC ferritic stainless steel. Depending on the interaction of the crack and the microstructure, these accumulated shear strain localisations take place inside the grains or at the grain boundaries, leading to the formation of grain sub-structures and consequent material hardening.

The main conclusions can be summarised as follows:

- FCG rate retardations correlate well with shear strain localisations, while the grain boundaries can be found both at peaks and valleys of the FCG rate curve;
- interaction between crack growth and shear strain localisations depends on their relative distance; if the shear strain localisation and the crack tip are in the same grain, retardation begins when the shear strain localisation starts to form; conversely, if they are in different grains, the GB has a shielding effect and retardation occurs only when the crack tip physically reaches the shear strain localisation;
- at the microstructural level, the shear strain localisation leads to the formation of grain sub-structures, i.e. dislocation cells and sub-grains; the sub-structures are local material hardened zones, and act as a local obstacle to crack growth;
- if the crack penetrates through the locally hardened material zone, the FCG rate has a significant retardation; instead, if the crack avoids the hardened material zone by macroscopic cross slip, the retardation is only minor;
- the macroscopic cross-slip directions were in agreement with the directions of dislocation motion for screw dislocations, with the growth directions showing agreement to both {1 1 0} and {2 1 1} slip planes.

Despite the enormous effort and contribution from the scientific community to tackle and model small and short crack propagation mechanisms, there are still many challenges and questions to be addressed. The present study focused on the FCG rate variation and the formation of grain sub-structures induced by shear strain localisations, and to establish the main mechanisms. The stochastic aspects of interaction between e.g., the crack tip, strain localisations and crystallographic orientation still need to be considered both experimentally and numerically, and it is left for future work.

The integration of new or improved technologies (e.g. high-resolution DIC, in situ small-scale testing, machine learning, advanced microstructural analyses) in this field of research is probably the key factor for enabling the next breakthrough.

CRediT authorship contribution statement

P. Gallo: Writing – original draft, Formal analysis, Investigation, Funding acquisition, Methodology, Software, Validation, Visualization. **P. Lehto:** Formal analysis, Writing – original draft, Investigation, Software, Visualization. **E. Malitckii:** Investigation. **H. Remes:** Supervision, Funding acquisition.

Declaration of Competing Interest

The authors declare that they have no known competing financial interests or personal relationships that could have appeared to influence the work reported in this paper.

Acknowledgements

Funding: This work was supported by the Academy of Finland [grant number 321244] and [grant number 298762].

We greatly appreciate the support provided by Ilari Tillikainen (Aalto University).

Appendix A. Details of microstructural analyses

A.1 Polishing process

The nickel-plated material section was mounted in an electrically conductive resin and ground using P320-P2000 grit abrasive papers, followed by polishing with 9 μm, 3 μm and 1 μm diamond paste. Fine polishing was carried out with 0.25 μm diamond paste, followed polished according to standard procedures and finalised by colloidal silica polishing in a vibratory polisher to minimise the deformation induced by the sample preparation process.

A.2 EBSD analyses

A Zeiss Ultra 55 field emission SEM equipped with a Nordlys F + EBSD detector and the Channel 5 software from Oxford Instruments were used for the measurements. The EBSD measurements were performed with a step size of 0.1–2 μm. The acceleration voltage was 20 kV and the working distance approximately 20.0 mm. A 120 μm aperture was used in conjunction with 4 × 4 detector binning to shorten the acquisition time of the patterns and reduce drift during the measurement. The patterns were acquired using an 8 ms exposure time, and the Hough resolution was set at 100. The number of bands for indexing was set from five to eight. The measurement noise of the EBSD datasets was estimated using the methodology proposed by Kamaya [82], implemented using MTEX [83,84] and available in [56]. The measurement noise level was quantified as approximately 0.35° for the datasets taken before and after the fatigue test, mapped at a 2 μm step size [42], and approximately 0.15° for the nickel-plated datasets, mapped at step sizes of 0.5 μm, 0.2 μm, and 0.1 μm. The EBSD analysis was carried out using MATLAB® [47] and MTEX version 5.6 [83,84]. Prior to the analyses the EBSD data was post-processed with the Half-Quadratic de-noising approach in MTEX according to the parameters presented in [24].

Appendix B. Supplementary material

Supplementary data to this article can be found online at https://doi.org/10.1016/j.ijfatigue.2022.107024.

References:

[1] Remes H, Romanoff J, Lillemäe I, Frank D, Liinalampi S, Lehto P, et al. Factors affecting the fatigue strength of thin-plates in large structures. Int J Fatigue 2017;101:397–407. https://doi.org/10.1016/j.ijfatigue.2016.11.019.

[2] Liinalampi S, Remes H, Lehto P, Lillemäe I, Romanoff J, Porter D. Fatigue strength analysis of laser-hybrid welds in thin plate considering weld geometry in microscale. Int J Fatigue 2016;87:143–52. https://doi.org/10.1016/j.ijfatigue.2016.01.019.

[3] Gallo P, Remes H, Romanoff J. Influence of crack tip plasticity on the slope of fatigue curves for laser stake-welded T-joints loaded under tension and bending. Int J Fatigue 2017;99:125–36. https://doi.org/10.1016/j.ijfatigue.2017.02.025.

[4] Gallo P, Guglielmo M, Romanoff J, Remes H. Influence of crack tip plasticity on fatigue behaviour of laser stake-welded T-joints made of thin plates. Int J Mech Sci 2018;136:112–23. https://doi.org/10.1016/j.ijmecsci.2017.12.011.

[5] Main B, Jones M, Barter S. The practical need for short fatigue crack growth rate models. Int J Fatigue 2021;142:105980. https://doi.org/10.1016/j.ijfatigue.2020.105980.

[6] Dowling NE. Mechanical Behavior of Materials: Engineering Methods for Deformation, Fracture, and Fatigue. 4th ed. Pearson; 2013.

[7] Suresh S, editor. Fatigue of Materials. Cambridge University Press; 1998.

[8] Davidson D, Chan K, McClung R, Hudak S. Small Fatigue Cracks. In: Milne I, Ritchie RO, Karihaloo BBT-CSI, editors. Compr. Struct. Integr., Oxford: Elsevier; 2003, p. 129–64. doi:10.1016/B0-08-043749-4/04073-8.

[9] Ravichandran KS, Li X-D. Fracture mechanical character of small cracks in polycrystalline materials: concept and numerical K calculations. Acta Mater 2000;48(2):525–40. https://doi.org/10.1016/S1359-6454(99)00348-1.

[10] Suresh S, Ritchie RO. Propagation of short fatigue cracks. Int Met Rev 1984;29(1):445–75. https://doi.org/10.1179/imtr.1984.29.1.445.

[11] Ritchie RO, Lankford J. Small fatigue cracks: A statement of the problem and potential solutions. Mater Sci Eng 1986;84:11–6. https://doi.org/10.1016/0025-5416(86)90217-X.

[12] Hussain K. Short fatigue crack behaviour and analytical models: A review. Eng Fract Mech 1997;58(4):327–54. https://doi.org/10.1016/S0013-7944(97)00102-1.

[13] Santus C, Taylor D. Physically short crack propagation in metals during high cycle fatigue. Int J Fatigue 2009;31(8-9):1356–65. https://doi.org/10.1016/j.ijfatigue.2009.03.002.

[14] McDowell DL. An engineering model for propagation of small cracks in fatigue. Eng Fract Mech 1997;56(3):357–77.

[15] Shyam A, Allison JE, Szczepanski CJ, Pollock TM, Jones JW. Small fatigue crack growth in metallic materials: A model and its application to engineering alloys. Acta Mater 2007;55(19):6606–16. https://doi.org/10.1016/j.actamat.2007.08.022.

[16] Brockman RA, Hoffman RM, Golden PJ, Musinski WD, Jha SK, John R. A computational framework for microstructural crack propagation. Int J Fatigue 2021;152:106397. https://doi.org/10.1016/j.ijfatigue.2021.106397.

[17] Rovinelli A, Sangid MD, Proudhon H, Ludwig W. Using machine learning and a data-driven approach to identify the small fatigue crack driving force in polycrystalline materials. Npj Comput Mater 2018;4:35. https://doi.org/10.1038/s41524-018-0094-7.

[18] Jones R, Singh Raman RK, McMillan AJ. Crack growth: Does microstructure play a role? Eng Fract Mech 2018;187:190–210. https://doi.org/10.1016/j.engfracmech.2017.11.023.

[19] Chapetti MD. Fracture mechanics for fatigue design of metallic components and small defect assessment. Int J Fatigue 2022;154:106550. https://doi.org/10.1016/j.ijfatigue.2021.106550.

[20] Tong J. Full-field characterisation of crack tip deformation and fatigue crack growth using digital image correlation—a review. Fatigue Fract Eng Mater Struct 2018;41(9):1855–69. https://doi.org/10.1111/ffe.12859.

[21] Orozco-Caballero A, Jackson T, da Fonseca JQ. High-resolution digital image correlation study of the strain localization during loading of a shot-peened RR1000 nickel-based superalloy. Acta Mater 2021;220:117306. https://doi.org/10.1016/j.actamat.2021.117306.

[22] Hémery S, Stinville JC, Wang F, Charpagne MA, Emigh MG, Pollock TM, et al. Strain localization and fatigue crack formation at (0001) twist boundaries in titanium alloys. Acta Mater 2021;219:117227. https://doi.org/10.1016/j.actamat.2021.117227.

[23] Matsushita A, Ueki S, Mine Y, Takashima K. Comparative Study of Microstructure-sensitive Fatigue Crack Propagation in Coarse- and Fine-grained Microstructures between Stable and Metastable Austenitic Stainless Steels Using Miniature Specimen. ISIJ Int 2021;61(5):1688–97. https://doi.org/10.2355/isijinternational.ISIJINT-2020-659.

[24] Lehto P. Adaptive domain misorientation approach for the EBSD measurement of deformation induced dislocation sub-structures. Ultramicroscopy 2021;222:113203. https://doi.org/10.1016/j.ultramic.2021.113203.

[25] Rollett AD, Wagner F, Allain-Bonasso N, Field DP, Lebensohn RA. Comparison of Gradients in Orientation and Stress between Experiment and Simulation. Mater Sci Forum 2011;702–703:463–8. https://doi.org/10.4028/www.scientific.net/MSF.702-703.463.

[26] Wright SI, Nowell MM, Field DP. A Review of Strain Analysis Using Electron Backscatter Diffraction. Microsc Microanal 2011;17(3):316–29. https://doi.org/10.1017/S1431927611000055.

[27] Sun S, Adams BL, King WE. Observations of lattice curvature near the interface of a deformed aluminium bicrystal. Philos Mag A Phys Condens Matter, Struct Defects Mech Prop 2000;80(1):9–25. https://doi.org/10.1080/01418610008212038.

[28] Tóth LS, Estrin Y, Lapovok R, Gu C. A model of grain fragmentation based on lattice curvature. Acta Mater 2010;58(5):1782–94. https://doi.org/10.1016/j.actamat.2009.11.020.

[29] Eshelby JD, Frank FC, Nabarro FRN. The equilibrium of linear arrays of dislocations. London, Edinburgh, Dublin Philos Mag J Sci 1951;42:351–64. https://doi.org/10.1080/14786445108561060.

[30] Hall EO. The deformation and ageing of mild steel: III Discussion of results. Proc Phys Soc 1951;64(9):747–53.

[31] Petch NJ. The cleavage strength of polycrystals. J Iron Steel Inst 1953;174:25–8.

[32] Muránsky O, Balogh L, Tran M, Hamelin CJ, Park JS, Daymond MR. On the measurement of dislocations and dislocation substructures using EBSD and HRSD techniques. Acta Mater 2019;175:297–313. https://doi.org/10.1016/j.actamat.2019.05.036.

[33] Tao NR, Wang ZB, Tong WP, Sui ML, Lu J, Lu K. An investigation of surface nanocrystallization mechanism in Fe induced by surface mechanical attrition treatment. Acta Mater 2002;50(18):4603–16. https://doi.org/10.1016/S1359-6454(02)00310-5.

[34] Gutierrez-Urrutia I, Raabe D. Dislocation and twin substructure evolution during strain hardening of an Fe–22wt.% Mn–0.6wt.% C TWIP steel observed by electron channeling contrast imaging. Acta Mater 2011;59(16):6449–62. https://doi.org/10.1016/j.actamat.2011.07.009.

[35] Kuhlmann-Wilsdorf D. Theory of plastic deformation: - properties of low energy dislocation structures. Mater Sci Eng A 1989;113:1–41. https://doi.org/10.1016/0921-5093(89)90290-6.

[36] Carroll JD, Abuzaid W, Lambros J, Sehitoglu H. High resolution digital image correlation measurements of strain accumulation in fatigue crack growth. Int J Fatigue 2013;57:140–50. https://doi.org/10.1016/j.ijfatigue.2012.06.010.

[37] Carroll JD, Abuzaid WZ, Lambros J, Sehitoglu H. On the interactions between strain accumulation, microstructure, and fatigue crack behavior. Int J Fract 2013;180(2):223–41. https://doi.org/10.1007/s10704-013-9813-8.

[38] Jiang R, Pierron F, Octaviani S, Reed PAS. Characterisation of strain localisation processes during fatigue crack initiation and early crack propagation by SEM-DIC

in an advanced disc alloy. Mater Sci Eng A 2017;699:128–44. https://doi.org/10.1016/j.msea.2017.05.091.

[39] Wilson D, Zheng Z, Dunne FPE. A microstructure-sensitive driving force for crack growth. J Mech Phys Solids 2018;121:147–74. https://doi.org/10.1016/j.jmps.2018.07.005.

[40] Chen B, Jiang J, Dunne FPE. Is stored energy density the primary meso-scale mechanistic driver for fatigue crack nucleation? Int J Plast 2018;101:213–29. https://doi.org/10.1016/j.ijplas.2017.11.005.

[41] Xu Y, Wan W, Dunne FPE. Microstructural fracture mechanics: Stored energy density at fatigue cracks. J Mech Phys Solids 2021;146:104209. https://doi.org/10.1016/j.jmps.2020.104209.

[42] Malitckii E, Remes H, Lehto P, Yagodzinskyy Y, Bossuyt S, Hänninen H. Strain accumulation during microstructurally small fatigue crack propagation in bcc Fe-Cr ferritic stainless steel. Acta Mater 2018;144:51–9. https://doi.org/10.1016/j.actamat.2017.10.038.

[43] Bossuyt S. Optimized Patterns for Digital Image Correlation. In: Jin H, Sciammarella C, Furlong C, Yoshida S, editors. Imaging Methods Nov. Mater. Challenging Appl. Vol. 3, New York, NY: Springer New York; 2013, p. 239–48.

[44] Coren F, Palestini C, Lehto M, Bossuyt S, Kiviluoma P, Korhonen A, et al. Microcontact printing on metallic surfaces for optical deformation measurements. Proc Est Acad Sci 2017;66(2):184. https://doi.org/10.3176/proc.2017.2.07.

[45] Malitckii E, Remes H, Lehto P, Bossuyt S. Full-field Strain Measurements for Microstructurally Small Fatigue Crack Propagation Using Digital Image Correlation Method. J Vis Exp 2019. https://doi.org/10.3791/59134.

[46] ASTM E647-15e1, Standard Test Method for Measurement of Fatigue Crack Growth Rates. West Conshohocken, PA: ASTM International; 2015. doi:10.1520/E0647-15E01.

[47] MATLAB. 9.5.0.1298439 (R2018b). Natick, Massachusetts: The MathWorks Inc.; 2018.

[48] MATLAB Curve Fitting Toolbox. Natick, Massachusetts, United State: The MathWorks Inc.; 2020.

[49] Larsen J, Allison J. Small-Crack Test Methods. West Conshohocken, PA: ASTM International; 1992. doi:10.1520/STP1149-EB.

[50] Larsen J. An Automated Photomicroscopic System for Monitoring the Growth of Small Fatigue Cracks. In: Underwood J, Chait R, Smith C, Wilhem D, Andrews W, Newman J, editors. Fract. Mech. Seventeenth Vol., West Conshohocken, PA: ASTM International: ASTM International; 1986, p. 226–38. doi:10.1520/STP17398S.

[51] Lehto P, Remes H, Saukkonen T, Hänninen H, Romanoff J. Influence of grain size distribution on the Hall-Petch relationship of welded structural steel. Mater Sci Eng A 2014;592:28–39. https://doi.org/10.1016/j.msea.2013.10.094.

[52] Lehto P, Romanoff J, Remes H, Sarikka T. Characterisation of local grain size variation of welded structural steel. Weld World 2016;60(4):673–88. https://doi.org/10.1007/s40194-016-0318-8.

[53] Lehto P. Aalto University Wiki: Grain size measurement using Matlab 2017. https://wiki.aalto.fi/display/GSMUM/Grain+size+measurement+using+Matlab (accessed January 5, 2022).

[54] Lehto P. EBSD measurement and visualisation of grain size variation: MTEX implementation for linear intercept length method 2021. doi:10.5281/zenodo.5053377.

[55] Lehto P. Grain interaction in local plastic deformation of welded structural steel - Influence of length-scale on sub-grain deformation behaviour for polycrystalline BCC material. Aalto University; 2019.

[56] Lehto P. Aalto University Wiki: EBSD measurement of deformation induced dislocation sub-structures 2021. https://wiki.aalto.fi/display/EMDIDS/EBSD+measurement+of+deformation+induced+dislocation+sub-structures (accessed January 5, 2022).

[57] Marichal C, Van Swygenhoven H, Van Petegem S, Borca C. 110 Slip with 112 slip traces in bcc Tungsten. Sci Rep 2013;3:2547. https://doi.org/10.1038/srep02547.

[58] Cereceda D, Diehl M, Roters F, Raabe D, Perlado JM, Marian J. Unraveling the temperature dependence of the yield strength in single-crystal tungsten using atomistically-informed crystal plasticity calculations. Int J Plast 2016;78:242–65. https://doi.org/10.1016/j.ijplas.2015.09.002.

[59] Schmid E, Boas W, editors. Kristallplastizität. Berlin, Heidelberg: Springer Berlin Heidelberg; 1935.

[60] Peralta P, Dickerson R, Dellan N, Komandur K, Jameel MA. Effects of local grain orientation on fatigue crack growth in multicrystalline fee metallic materials. J Eng Mater Technol Trans ASME 2005;127:23–32. https://doi.org/10.1115/1.1836768.

[61] Malitckii E, Yagodzinskyy Y, Lehto P, Remes H, Romu J, Hänninen H. Hydrogen effects on mechanical properties of 18%Cr ferritic stainless steel. Mater Sci Eng A 2017;700:331–7. https://doi.org/10.1016/j.msea.2017.06.028.

[62] McClintock FA. On the Plasticity of the Growth of Fatigue Cracks. Fract. Solids, New York: John Wiley & Sons Inc.; 1963.

[63] Newman JC, Phillips EP, Swain MH. Fatigue-life prediction methodology using small-crack theory. Int J Fatigue 1999;21:109–19. https://doi.org/10.1016/S0142-1123(98)00058-9.

[64] Pearson S. Initiation of fatigue cracks in commercial aluminium alloys and the subsequent propagation of very short cracks. Eng Fract Mech 1975;7(2):235–47.

[65] Lankford J. On the small crack fracture mechanics problem. Int J Fract 1980;16(1):R7–9. https://doi.org/10.1007/BF00042389.

[66] Ye S, Zhang X-C, Gong J-G, Tu S-T, Zhang C-C. Multi-scale fatigue crack propagation in 304 stainless steel: experiments and modelling. Fatigue Fract Eng Mater Struct 2017;40:1928–41. https://doi.org/10.1111/ffe.12615.

[67] Musinski WD, McDowell DL. Simulating the effect of grain boundaries on microstructurally small fatigue crack growth from a focused ion beam notch through a three-dimensional array of grains. Acta Mater 2016;112:20–39. https://doi.org/10.1016/j.actamat.2016.04.006.

[68] Zhai T, Wilkinson AJ, Martin JW. A crystallographic mechanism for fatigue crack propagation through grain boundaries. Acta Mater 2000;48(20):4917–27. https://doi.org/10.1016/S1359-6454(00)00214-7.

[69] Schaef W, Marx M, Vehoff H, Heckl A, Randelzhofer P. A 3-D view on the mechanisms of short fatigue cracks interacting with grain boundaries. Acta Mater 2011;59(5):1849–61. https://doi.org/10.1016/j.actamat.2010.11.051.

[70] Hansson P, Melin S. Grain boundary influence on short fatigue crack growth rate. Int J Fract 2010;165(2):199–210. https://doi.org/10.1007/s10704-010-9512-7.

[71] Zhang XP, Wang CH, Ye L, Mai YW. In situ investigation of small fatigue crack growth in poly-crystal and single-crystal aluminium alloys. Fatigue Fract Eng Mater Struct 2002;25:141–50. https://doi.org/10.1046/j.8756-758x.2001.00484.x.

[72] Luster J, Morris MA. Compatibility of deformation in two-phase Ti-Al alloys: Dependence on microstructure and orientation relationships. Metall Mater Trans A 1995;26(7):1745–56. https://doi.org/10.1007/BF02670762.

[73] McEvily AJ, Johnston TL. The role of cross-slip in brittle fracture and fatigue. Int J Fract Mech 1967;3(1):45–74. https://doi.org/10.1007/BF00188645.

[74] Hobson PD. The formulation of a crack growth equation for short cracks. Fatigue Fract Eng Mater Struct 1982;5(4):323–7. https://doi.org/10.1111/j.1460-2695.1982.tb01241.x.

[75] Chan KS, Lankford J. A crack-tip strain model for the growth of small fatigue cracks. Scr Metall 1983;17(4):529–32. https://doi.org/10.1016/0036-9748(83)90346-0.

[76] Navarro A, Rios ER. A microstructurally-short fatigue crack growth equation. Fatigue Fract Eng Mater Struct 1988;11(5):383–96. https://doi.org/10.1111/j.1460-2695.1988.tb01391.x.

[77] Remes H, Gallo P, Jelovica J, Romanoff J, Lehto P. Fatigue strength modelling of high-performing welded joints. Int J Fatigue 2020;135:105555. https://doi.org/10.1016/j.ijfatigue.2020.105555.

[78] Tang K, Du Z, Wu B, Hou J. Fatigue behavior prediction of metal alloys based on a unified multiscale crack growth model. Eng Fract Mech 2020;235:107132. https://doi.org/10.1016/j.engfracmech.2020.107132.

[79] Remes H, Varsta P, Romanoff J. Continuum approach to fatigue crack initiation and propagation in welded steel joints. Int J Fatigue 2012;40:16–26. https://doi.org/10.1016/j.ijfatigue.2012.01.007.

[80] Gallo P, Hagiwara Y, Shimada T, Kitamura T. Strain energy density approach for brittle fracture from nano to macroscale and breakdown of continuum theory. Theor Appl Fract Mech 2019;103:102300. https://doi.org/10.1016/j.tafmec.2019.102300.

[81] Lubich S, Fischer C, Schilli S, Seifert T. Microstructure-sensitive finite-element analysis of crack-tip opening displacement and crack closure for microstructural short fatigue cracks. Int J Fatigue 2022;162:106911. https://doi.org/10.1016/j.ijfatigue.2022.106911.

[82] Kamaya M. Assessment of local deformation using EBSD: Quantification of accuracy of measurement and definition of local gradient. Ultramicroscopy 2011;111(8):1189–99. https://doi.org/10.1016/j.ultramic.2011.02.004.

[83] Bachmann F, Hielscher R, Schaeben H. Texture analysis with MTEX- Free and open source software toolbox. Solid State Phenom 2010;160:63–8. https://doi.org/10.4028/www.scientific.net/SSP.160.63.

[84] Nolze G, Hielscher R. IPF coloring of crystal orientation data. J Appl Crystallogr 2016.